ATLAS NOTE

ATLAS-CONF-2013-049

May 13, 2013,
Revision: August 19, 2013

Searches for direct slepton-pair and chargino-pair production in final states with two opposite-sign leptons, missing transverse momentum and no jets in $20\,\mathrm{fb}^{-1}$ of pp collisions at $\sqrt{s} = 8$ TeV with the ATLAS detector

The ATLAS Collaboration

Abstract

Searches for the electroweak production of pairs of sleptons or charginos decaying into final states with two leptons, missing transverse momentum and no reconstructed jets are performed using $20.3\,\mathrm{fb}^{-1}$ of proton-proton collision data at $\sqrt{s} = 8$ TeV recorded with the ATLAS experiment at the Large Hadron Collider. No significant excesses are observed with respect to the prediction from Standard Model processes. Limits are set on the masses of the slepton and of the lightest chargino for different lightest-neutralino mass hypotheses. In scenarios where sleptons decay directly into the lightest neutralino and a charged lepton, common values for left and right-handed slepton masses between $90\,\mathrm{GeV}$ and $320\,\mathrm{GeV}$ are excluded at 95% confidence level for a massless neutralino. In the scenario of chargino pair production, with wino-like charginos decaying into the lightest neutralino via an intermediate slepton, chargino masses between $130\,\mathrm{GeV}$ and $450\,\mathrm{GeV}$ are excluded at 95% confidence level for a 20 GeV neutralino. In the scenario of chargino pair production followed by the $\tilde{\chi}_1^\pm \rightarrow W^\pm \tilde{\chi}_1^0$ decay, the excluded cross-section is above the model cross-section by a factor 1.9–2.8 in the $\tilde{\chi}_1^\pm$ mass range of 100–190 GeV and then degrades gradually to 4.7 when reaching a $\tilde{\chi}_1^\pm$ mass of 250 GeV.

The following has been revised with respect to the version dated May 13, 2013: in Table 7, the expected number of signal events at the SR-$m_{\mathrm{T2,110}}$ cut level for the $e^\pm \mu^\mp$ channel for the benchmark model point $(m_{\tilde{\chi}_1^\pm}, m_{\tilde{\chi}_1^0}) = (425, 75)$ GeV has been changed to its correct value of 5.7 (previously 1.1).

1 Introduction

Weak-scale Supersymmetry (SUSY) [1–9] is an extension to the Standard Model (SM) of particle physics. It postulates for each known boson or fermion the existence of a particle whose spin differs by one-half unit from the SM partner. The introduction of these new particles provides solutions to the hierarchy problem [10–13] and, if R-parity is conserved [14–18], a dark matter candidate in the form of the lightest supersymmetric particle (LSP). R-parity conservation is assumed in this note, hence SUSY particles are always produced in pairs.

If the masses of the gluinos and squarks are large, the direct production of charginos, neutralinos and sleptons may dominate the production of SUSY particles at the Large Hadron Collider (LHC) [19]. Such a scenario is possible in the general framework of the phenomenological minimal supersymmetric SM (pMSSM) [20–22]. Naturalness suggests that third-generation sparticles, charginos and neutralinos should have masses of a few hundreds of GeV [23, 24]. Light sleptons are expected in gauge-mediated [25–30] and anomaly-mediated [31, 32] SUSY breaking scenarios. Light sleptons could also play a role in the co-annihilation of neutralinos, leading to a dark matter relic density consistent with cosmological observations [33, 34].

This note presents searches for electroweak production of sleptons and charginos using $20.3\,\mathrm{fb}^{-1}$ of $\sqrt{s} = 8$ TeV pp collision data collected with the ATLAS detector. Similar searches have previously been performed by the ATLAS experiment using $4.7\,\mathrm{fb}^{-1}$ of 7 TeV data [35], and by the CMS experiment using $9.2\,\mathrm{fb}^{-1}$ of 8 TeV data [36]. A related ATLAS search was also performed at 8 TeV [37]. The combined LEP limits on the selectron, smuon and chargnino masses are $m_{\tilde{e}} > 99.9$ GeV, $m_{\tilde{\mu}} > 94.6$ GeV and $m_{\tilde{\chi}_1^\pm} > 103.5$ GeV [38]. Note that the LEP selectron limit assumes gaugino mass unification and cannot be directly compared with the results presented in this note.

The searches presented in this note target the following four scenarios that produce final states with two oppositely-charged leptons (electrons or muons) and missing transverse momentum.

Sleptons can be produced directly in a process similar to Drell-Yan production [39]. The direct pair production of charged sleptons, $q\bar{q} \to \tilde{\ell}^+\tilde{\ell}^-$ is considered, where each slepton decays through $\tilde{\ell}^\pm \to \ell^\pm\tilde{\chi}_1^0$. The undetected neutralinos give rise to large missing transverse momentum in the event.

Direct chargino-pair production through weak interactions, $q\bar{q} \to \tilde{\chi}_1^+\tilde{\chi}_1^-$, where each chargino decays through $\tilde{\chi}_1^\pm \to (\tilde{\ell}^\pm\nu$ or $\ell^\pm\tilde{\nu}) \to \ell^\pm\nu\tilde{\chi}_1^0$ leads to a signature similar to that of the direct slepton pair production, even though two additional neutrinos contribute to the missing transverse momentum. Unlike the direct slepton production, the final state leptons can be either of the same flavour (e^+e^- or $\mu^+\mu^-$) or of different flavours ($e^\pm\mu^\mp$).

If the lightest chargino is the NLSP, the chargino decays as $\tilde{\chi}_1^\pm \to W^\pm\tilde{\chi}_1^0$, producing an on- or off-shell W boson. If both W bosons decay leptonically, the final state will again contain two opposite-sign leptons and large missing transverse momentum due to the presence of two neutrinos and two neutralinos. Although the leptons can be of either the same or different flavours, this analysis uses only the $e^\pm\mu^\mp$ channel because of the smaller background.

The gauge-mediated SUSY breaking (GMSB) model proposed in Ref. [40] is also considered. The search strategy is the same as for the channel with two on-shell W bosons, and so only the $e^\pm\mu^\mp$ channel is considered.

2 The ATLAS Detector

The ATLAS experiment [41] is a multi-purpose particle physics detector with a forward-backward symmetric cylindrical geometry and nearly 4π coverage in solid angle[1]. It contains four superconducting

---

[1] ATLAS uses a right-handed coordinate system with its origin at the nominal interaction point in the centre of the detector and the z-axis along the beam pipe. Cylindrical coordinates (r, ϕ) are used in the transverse plane, ϕ being the azimuthal angle

magnet systems, which include a thin solenoid surrounding the inner tracking detector (ID), and barrel and end-cap toroids supporting a muon spectrometer. The ID covers the pseudorapidity region $|\eta| < 2.5$ and consists of a silicon pixel detector, a silicon microstrip detector (SCT), and a transition radiation tracker (TRT). In the pseudorapidity region $|\eta| < 3.2$, high-granularity liquid-argon (LAr) electromagnetic (EM) sampling calorimeters are used. An iron-scintillator tile calorimeter provides coverage for hadron detection over $|\eta| < 1.7$. The end-cap and forward regions, spanning $1.5 < |\eta| < 4.9$, are instrumented with LAr calorimeters for both EM and hadronic measurements. The muon spectrometer surrounds the calorimeters and consists of a system of precision tracking chambers ($|\eta| < 2.7$), and detectors for triggering ($|\eta| < 2.4$).

3   Data Samples

The data used in this analysis were collected during the 2012 proton-proton collision run at $\sqrt{s} = 8$ GeV. After applying beam, detector and data-quality requirements, the dataset corresponds to a total integrated luminosity of $20.3\,\text{fb}^{-1}$.

Events are triggered using two-lepton triggers. There are two dielectron triggers with the leading and sub-leading lepton p_T thresholds of $(14, 14)$ GeV and $(25, 8)$ GeV, and two dimuon triggers with the p_T thresholds of $(14, 14)$ GeV and $(18, 8)$ GeV. Additionally, two electron-muon triggers with $(p_\text{T}^e, p_\text{T}^\mu) > (14, 8)$ GeV and $(8, 18)$ GeV are used. The dielectron triggers have efficiencies ranging between 85% and 98%, where the lowest efficiency comes from the asymmetric dielectron trigger in the end-cap region. The dimuon triggers have efficiencies ranging between 52% (77%) and 80% (98%) in the barrel (end-caps), where the lowest efficiency trigger comes from the symmetric dimuon trigger. The asymmetric electron-muon triggers have efficiencies ranging between 65% and 82%. All quoted efficiencies have been measured in data with respect to reconstructed leptons with p_T in excess of the nominal thresholds.

Monte Carlo (MC) simulated event samples are used to develop and validate the analysis procedure and to evaluate the SM backgrounds. The predictions for the most relevant SM processes are normalised in dedicated control regions, as detailed in Section 6. All MC samples are produced using a `GEANT4` [42] based detector simulation [43–45]. The effect of multiple proton-proton collisions from the same or different bunch crossings is incorporated into the simulation by overlaying minimum bias events onto hard scatter events using `PYTHIA` [46]. Simulated events are weighted to match the distribution of the number of interactions per bunch crossing observed in data.

The dominant SM background processes include $WW \rightarrow \ell\nu\ell\nu$, $t\bar{t}$, single-top, and ZV where $V = W$ or Z. Production of top quark pairs is simulated with `MC@NLO` [47–49] using a top-quark mass of 172.5 GeV. Additional samples generated with `POWHEG` [50] plus `PYTHIA` and `ALPGEN` [51] plus `HERWIG` [52] are used for the evaluation of systematic uncertainties. The $t\bar{t}$ cross-section is normalised to approximate next-to-next-to-leading order (NNLO) calculations [53]. Single top production is modelled with `MC@NLO` for Wt and s-channel production, and with `AcerMC` [54] for t-channel production. Samples of $W \rightarrow \ell\nu$ and $Z/\gamma^* \rightarrow \ell\ell$ produced with accompanying jets (including light and heavy flavours) are obtained with a combination of `SHERPA` [55] and `ALPGEN`. The inclusive W and Z/γ^* production cross-sections are normalised to the NNLO cross-sections obtained using `DYNNLO` [56]. Diboson (WW, WZ and ZZ) production is simulated with `POWHEG`, with additional gluon-gluon contributions simulated with `gg2WW` [57] and `gg2ZZ` [58]. Additional diboson samples are generated with `SHERPA` to assess systematic uncertainties. The diboson cross-sections are normalised using next-to-leading order (NLO) QCD predictions obtained with `MCFM` [59, 60]. Production of $t\bar{t}$ associated with a vector boson is simulated with the leading-order (LO) generator `MADGRAPH` [61] and scaled to the NLO cross-section [62–64]. QCD production of $b\bar{b}$ and $c\bar{c}$ is simulated with `PYTHIA`. Finally, production of the SM Higgs with $m_H = 125$ GeV

---

around the beam pipe. The pseudorapidity η is defined in terms of the polar angle θ by $\eta = -\ln\tan(\theta/2)$.

through gluon fusion, vector-boson fusion and associated Higgs production (*WH* and *ZH*) is considered. The associated production modes are generated with `PYTHIA`, while `POWHEG` is used for the others.

Fragmentation and hadronisation for the `MC@NLO` and `ALPGEN` samples are performed either with `HERWIG` using `JIMMY` [65] for the underlying event, or with `PYTHIA`. `PYTHIA` is used for the `POWHEG` and `MADGRAPH` samples. The CT10 NLO [66] and CTEQ6L1 [67] parton-distribution function sets are used with the NLO and LO event generators, respectively.

Simulated signal samples are generated with `HERWIG++` [68]. Signal cross-sections are calculated at NLO using `PROSPINO2` [69].

Direct-slepton scenario The direct-slepton models are based on the pMSSM and described in Ref. [70]. The masses of all charginos and neutralinos apart from the $\tilde{\chi}_1^0$ are set to 2.5 TeV. The sensitivity of the present search is determined for models with varying slepton and $\tilde{\chi}_1^0$ masses. The mass of the bino-like $\tilde{\chi}_1^0$ is varied by scanning the gaugino mass parameter M_1 in the range 0–200 GeV. The common selectron and smuon mass is generated in the range 90–370 GeV with the constraint $m_{\tilde{\ell}} \geq m_{\tilde{\chi}_1^0} + 30$ GeV. The cross-section for direct slepton pair production (per slepton flavour) in these models decreases from 127 to 0.5 fb for left-handed sleptons, and from 49 to 0.2 fb for right-handed sleptons, as the slepton mass increases from 90 to 370 GeV.

Chargino-to-slepton scenario The chargino-to-slepton decays are simulated in simplified models, in the scenario of charginos decaying into the lightest neutralino via an intermediate on-shell charged slepton, in which the masses of $\tilde{\chi}_1^0$, $\tilde{\ell}$, $\tilde{\nu}$ and $\tilde{\chi}_1^\pm$ are the only free parameters. The squarks are assumed to be well beyond the kinematical reach. The $\tilde{\chi}_1^\pm$ are pair-produced via the *s*-channel exchange of a virtual gauge boson and decay via left-handed sleptons, including $\tilde{\tau}$ and $\tilde{\nu}$, of mass $m_{\tilde{\ell}} = m_{\tilde{\nu}} = (m_{\tilde{\chi}_1^0} + m_{\tilde{\chi}_1^\pm})/2$ with equal branching ratios. The cross-section for $\tilde{\chi}_1^\pm \tilde{\chi}_1^\mp$ pair production calculated under the assumption that the chargino is 95% wino-like (with a small higgsino component), is as high as 5 pb for a chargino mass of 100 GeV and decreases rapidly at higher masses, reaching 9 fb at 450 GeV.

Chargino-to-*W* scenario Simulated samples for chargino-to-*W* decays, where the sleptons are mass decoupled, were also produced with simplified models. The mass grid spans the $m_{\tilde{\chi}_1^\pm}$ vs. $m_{\tilde{\chi}_1^0}$ plane in 10-GeV steps on both axes starting from $(m_{\tilde{\chi}_1^\pm}, m_{\tilde{\chi}_1^0}) = (100, 0)$ GeV (close to the LEP limit [38]) and keeping $m_{\tilde{\chi}_1^\pm} - m_{\tilde{\chi}_1^0} > 80$ GeV. The cross-section used for $\tilde{\chi}_1^\pm \tilde{\chi}_1^\mp$ pair production is the same as for the chargino-to-slepton scenario. The branching ratio of $\tilde{\chi}_1^\pm \to W^\pm \tilde{\chi}_1^0$ is assumed to be 100%.

GMSB model An additional simplified model sample is generated to probe the GMSB model proposed in Ref. [40]. In this model, the LSP is the gravitino $\tilde{G}$, the NLSP is the chargino with $m_{\tilde{\chi}_1^\pm} = 110$ GeV, and in addition there are two other light neutralinos $m_{\tilde{\chi}_1^0} = 113$ GeV and $m_{\tilde{\chi}_2^0} = 130$ GeV. All coloured sparticle are assumed to be very heavy. Although the $\tilde{\chi}_1^+ \tilde{\chi}_1^-$ production cross-section is not large ($\sim$1.4 pb), it is augmented by the $\tilde{\chi}_1^\pm \tilde{\chi}_1^0$ ($\sim$2.5 pb), $\tilde{\chi}_1^\pm \tilde{\chi}_2^0$ ($\sim$1.0 pb) and $\tilde{\chi}_1^0 \tilde{\chi}_2^0$ ($\sim$0.5 pb). The $\tilde{\chi}_1^0$ decays 100% into $\tilde{\chi}_1^\pm W^{\mp*}$, and the $\tilde{\chi}_2^\pm$ decays either into $\tilde{\chi}_1^\pm W^{\mp*}$ or $\tilde{\chi}_1^0 Z^*$. Because of the small mass differences, the decay products of the off-shell *W* and *Z* bosons are unlikely to be detected. As a result, all of the four production channels result in the same experimental signature, and their production cross-sections can be added together for the purpose of this search. Each $\tilde{\chi}_1^\pm$ then decays 100% via $\tilde{\chi}_1^\pm \to W^\pm \tilde{G}$, and leptonic decays of the two the on-shell *W* bosons produce the same final-state as in the chargino-to-*W* scenario above.

4 Event Selection

Events are selected in which at least five charged tracks are associated to the primary vertex. If there are multiple primary vertices in an event, the one with the largest $\sum p_T^2$ of the associated tracks is chosen. In each event, "candidate" electrons, muons, and jets are constructed. After removing potential overlaps between these objects, the criteria to define "signal" electrons, muons, and jets are refined.

Electron candidates are reconstructed by matching clusters in the EM calorimeter with charged tracks in the ID. They are required to have $p_T > 10$ GeV, $|\eta| < 2.47$, and pass the "medium" shower-shape and track-selection criteria defined in Ref. [71].

Muon candidates are reconstructed by matching a muon spectrometer track to an ID track. They are then required to have $p_T > 10$ GeV and $|\eta| < 2.4$. They must be reconstructed with sufficient hits in the pixel, SCT and TRT detectors.

Jet candidates are reconstructed using the anti-k_T jet clustering algorithm [72, 73] with a distance parameter of 0.4. The jet candidates are corrected for the effects of calorimeter non-compensation and inhomogeneities by using p_T and η-dependent calibration factors based on MC simulation and validated with extensive test-beam and collision-data studies [74]. Only jet candidates with $p_T > 20$ GeV and $|\eta| < 4.5$ are subsequently retained. Events containing jets that are likely to have arisen from detector noise or cosmic rays are removed [74].

Object overlaps are defined in terms of $\Delta R = \sqrt{(\Delta\eta)^2 + (\Delta\phi)^2}$, where $\Delta\eta$ and $\Delta\phi$ are separations in η and ϕ. Objects are systematically removed so that no two lepton candidates are within $\Delta R = 0.1$ of each other (except for two muons for which the threshold is 0.05) and no lepton is within $\Delta R = 0.4$ of a jet.

Signal electrons must pass the "tight" criteria [71] placed on the ratio of calorimetric energy to track momentum, and the number of high-threshold hits in the TRT. They are also required to be isolated within the tracking volume and the calorimeter. The p_T sum of tracks above 400 MeV within a cone of size $\Delta R = 0.3$ around each electron candidate (excluding the electron candidate itself) is required to be less than 16% of the electron p_T. The transverse energies of the surrounding topological clusters within $\Delta R = 0.3$ of each electron candidate, corrected for deposition of energy from pile-up events, is required to be less than 18% of the electron transverse energy. The distance of closest approach of an electron candidate to the event primary vertex must be within five standard deviations in the transverse plane. The distance along the beam direction, z_0, must satisfy $|z_0| \sin\theta < 0.4$ mm.

Signal muons must also be isolated: the p_T sum of tracks above 1 GeV within a cone of size $\Delta R = 0.3$ around the muon candidate is required to be less than 12% of the muon p_T. The closest approach of a muon candidate to the event primary vertex must be within three standard deviations in the transverse plane, and $|z_0| \sin\theta < 1$ mm along the beam direction.

A b-tagging algorithm [75], which exploits the long lifetime of b- and c-hadron decays inside a candidate jet, is used to identify jets containing a b-hadron decay. The mean nominal b-tagging efficiency, determined from $t\bar{t}$ MC events, is 80%, with a misidentification (mis-tag) rate for light-quark/gluon jets of less than 1%. Scale factors (which depend on p_T and η) are applied to all MC samples to correct for small differences in the b-tagging performance observed between data and simulation.

Signal jets are classified in three exclusive categories; a jet fulfilling any of these categories is considered to be a signal jet. Central b-jets satisfy $|\eta| < 2.4$ and are identified as b-jets by the b-tagging algorithm. Central light-flavour jets also satisfy $|\eta| < 2.4$ but do not satisfy the b-jet identification criteria. If a central light-flavour jet has $p_T < 50$ GeV and has charged tracks associated to it, at least one of the tracks must originate from the event primary vertex. This criterion removes jets that originated in pile-up collisions. Finally, forward jets are those with $2.4 < |\eta| < 4.5$ and $p_T > 30$ GeV.

Having selected signal electrons, muons and jets, exactly two signal leptons of opposite charge and no signal jets of any category in the selected events are required. The two signal leptons are required to have triggered the event, and their p_T must be above the efficiency plateau threshold of the corresponding

trigger. The dilepton invariant mass $m_{\ell\ell}$ must be greater than 20 GeV in all flavour combinations. Events with one or more jets will be used in defining the $t\bar{t}$ control regions, described in Section 6.1.

The measurement of the missing transverse momentum two-vector, $\mathbf{p}_T^{\mathrm{miss}}$, and its magnitude, E_T^{miss}, is based on the transverse momenta of all electron and muon candidates, all jets, and all clusters of calorimeter energy with $|\eta| < 4.9$ not associated to such objects. The quantity $E_T^{\mathrm{miss,rel.}}$ is defined as:

$$
E_T^{\mathrm{miss,rel.}} = \left\{ \begin{array}{ll} E_T^{\mathrm{miss}} & \text{if } \Delta\phi_{\ell,j} \geq \pi/2 \\ E_T^{\mathrm{miss}} \times \sin \Delta\phi_{\ell,j} & \text{if } \Delta\phi_{\ell,j} < \pi/2 \end{array} \right. ,
$$

where $\Delta\phi_{\ell,j}$ is the azimuthal angle between the direction of $\mathbf{p}_T^{\mathrm{miss}}$ and that of the nearest electron, muon, central b-jet or central light-flavour jet. In a situation where the momentum of one of the jets or leptons is significantly mis-measured, such that it is aligned with the direction of $\mathbf{p}_T^{\mathrm{miss}}$, only the E_T^{miss} component perpendicular to that object is considered. This is used to significantly reduce mis-measured E_T^{miss} in processes such as $Z/\gamma^* \to \ell^+\ell^-$ [76].

The "stransverse" mass variable m_{T2} [77, 78] is defined as:

$$
m_{\mathrm{T2}} = \min_{\mathbf{q}_T} \left[\max \left(m_T(\mathbf{p}_T^{\ell 1}, \mathbf{q}_T), m_T(\mathbf{p}_T^{\ell 2}, \mathbf{p}_T^{\mathrm{miss}} - \mathbf{q}_T) \right) \right],
$$

where $\mathbf{p}_T^{\ell 1}$ and $\mathbf{p}_T^{\ell 2}$ are the transverse momenta of the two leptons, and $\mathbf{q}_T$ is a transverse vector that minimises the larger of the two transverse masses m_T. The latter is defined by

$$
m_T(\mathbf{p}_T, \mathbf{q}_T) = \sqrt{2(p_T q_T - \mathbf{p}_T \cdot \mathbf{q}_T)}.
$$

For $t\bar{t}$ and WW events, in which two on-shell W bosons decayed leptonically and $\mathbf{p}_T^{\mathrm{miss}}$ is the sum of two neutrinos, the m_{T2} distribution has an upper end-point at the W mass. For large mass differences between the sleptons (charginos) and the lightest neutralino, the m_{T2} distribution for signal events extends significantly beyond the distributions of the $t\bar{t}$ and WW events and so the end-point of this function contains information about this mass difference; additional missing momentum due to the LSPs also contributes to the m_{T2} distribution.

5 Signal Regions

Five signal regions (SRs) are defined in this analysis. The first two, referred to as SR-$m_{\mathrm{T2,90}}$ and SR-$m_{\mathrm{T2,110}}$, are designed to provide sensitivity to sleptons either through direct production or in chargino decays. The other three, SR-WWa, SR-WWb and SR-WWc, are designed to provide sensitivity to chargino- and neutralino-pair production followed by on-shell W decays. Table 1 summarises the definitions of the SRs.

5.1 SR-m_{T2}

In SR-m_{T2}, the properties of m_{T2} are exploited to search for $\tilde{\ell}^\pm \tilde{\ell}^\mp$ and $\tilde{\chi}_1^\pm \tilde{\chi}_1^\mp$ production followed by decay to final states containing exactly two opposite-sign leptons, no signal jets, and missing transverse momentum. Only same-flavour channels (e^+e^- and $\mu^+\mu^-$) are used in the search for direct slepton production, while the chargino-to-slepton decay search also uses $e^\pm\mu^\mp$. Their invariant mass $m_{\ell\ell}$ must be at least 10 GeV from the nominal Z boson mass to reduce the background from Z decays. Results from different channels are statistically combined through a maximum-likelihood fit.

In this signal region, WW, ZV, and $t\bar{t}$ are dominant sources of background. For large mass differences between the sleptons (charginos) and the lightest neutralino, the m_{T2} distribution for signal events extends beyond the distributions for $t\bar{t}$ and diboson backgrounds, since the neutralinos can be signficantly more

Table 1: Signal region definitions of events satisfying the selection of Section 4. 'Z veto' refers to $|m_{\ell\ell} - m_Z| > 10$ GeV.

	SR-$m_{T2,90}$	SR-$m_{T2,110}$	SR-WWa	SR-WWb	SR-WWc
lepton flavour	$e^+e^-, \mu^+\mu^-, e^\pm\mu^\mp$		$e^\pm\mu^\mp$		
$p_T^{\ell 1}$	—		> 35 GeV		
$p_T^{\ell 2}$	—		> 20 GeV		
$m_{\ell\ell}$	Z veto		< 80 GeV	< 130 GeV	—
$p_{T,\ell\ell}$	—		> 70 GeV	< 170 GeV	< 190 GeV
$\Delta\phi_{\ell\ell}$	—		< 1.8 rad		
$E_T^{\mathrm{miss,rel}}$	> 40 GeV		> 70 GeV	—	
m_{T2}	> 90 GeV	> 110 GeV	—	> 90 GeV	> 100 GeV

boosted than the neutrinos from the background sources. Two different requirements, $m_{T2} > 90$ GeV and $m_{T2} > 110$ GeV, are defined for SR-$m_{T2,90}$ and SR-$m_{T2,110}$, respectively. The former provides a better sensitivity to cases in which the slepton or chargino mass is close to the LSP mass, and the latter has a better coverage at larger slepton/chargino-LSP mass differences.

Figure 1 shows the distributions of $E_T^{\mathrm{miss,rel}}$ and m_{T2} satisfying the event selection of Section 4, and requiring $E_T^{\mathrm{miss,rel}} > 40$ GeV and the Z veto. Good agreement between data and Monte Carlo is observed for all variables and samples.

5.2 SR-WW

Three signal regions, SR-WWa, SR-WWb and SR-WWc, are designed to provide sensitivities to direct chargino and neutralino production with $\tilde{\chi}_1^\pm \rightarrow W^\pm + \tilde{\chi}_1^0$ in three different areas of the $m_{\tilde{\chi}_1^\pm}$ vs. $m_{\tilde{\chi}_1^0}$ plane. Only the $e^\pm\mu^\mp$ combinations are used in these signal regions.

Since the signal is assumed to produce a pair of on-shell W bosons, the signal-to-background ratio can be improved by requiring larger lepton p_T without large loss in acceptance. This would not be the case in the slepton scenarios with small slepton-neutralino mass differences or if the W boson is off-shell. The leading lepton is required to have $p_T > 35$ GeV and the other lepton to have $p_T > 20$ GeV.

Figure 2 shows the data to Monte Carlo agreement in the distributions of m_{T2}, $E_T^{\mathrm{miss,rel}}$, $m_{\ell\ell}$ and $p_{T,\ell\ell}$ (the transverse momentum of the dilepton system) after the selection described in Section 4 and the additional requirements on the the lepton p_T. The four variables are used to define the three signal regions.

The first region, SR-WWa, is designed for scenarios in which either the chargino mass is small ($m_{\tilde{\chi}_1^\pm} < 120$ GeV) or the W boson is produced close to the threshold ($m_W < m_{\tilde{\chi}_1^\pm} - m_{\tilde{\chi}_1^0} < 100$ GeV). In this signal region, $E_T^{\mathrm{miss,rel}} > 70$ GeV and $p_{T,\ell\ell} > 70$ GeV are required. These thresholds are found to be optimal to reject SM WW production efficiently while retaining SUSY signal events, characterised by larger transverse momentum of the LSPs. The sensitivity is further increased by requiring $m_{\ell\ell} < 80$ GeV, and the opening angle between the two leptons in the transverse plane $\Delta\phi_{\ell\ell}$ to be smaller than 1.8 radians.

The second and third regions, SR-WWb and SR-WWc, are sensitive to higher chargino masses ($m_{\tilde{\chi}_1^\pm} > 120$ GeV), and larger boost of the W boson ($m_{\tilde{\chi}_1^\pm} - m_{\tilde{\chi}_1^0} > 100$ GeV). These regions rely on the m_{T2} variable, which is required to be greater than 90 GeV and 100 GeV in SR-WWb and SR-WWc, respectively. Also required are $p_{T,\ell\ell} < 170$ GeV and < 190 GeV in SR-WWb and SR-WWc, respectively. The differences in the thresholds make SR-WWc more sensitive to larger chargino masses and larger W boost than SR-WWb. For SR-WWb, $m_{\ell\ell} < 130$ GeV is also required. Finally, the same $\Delta\phi_{\ell\ell} < 1.8$ rad cut as SR-WWa is applied to both signal regions.
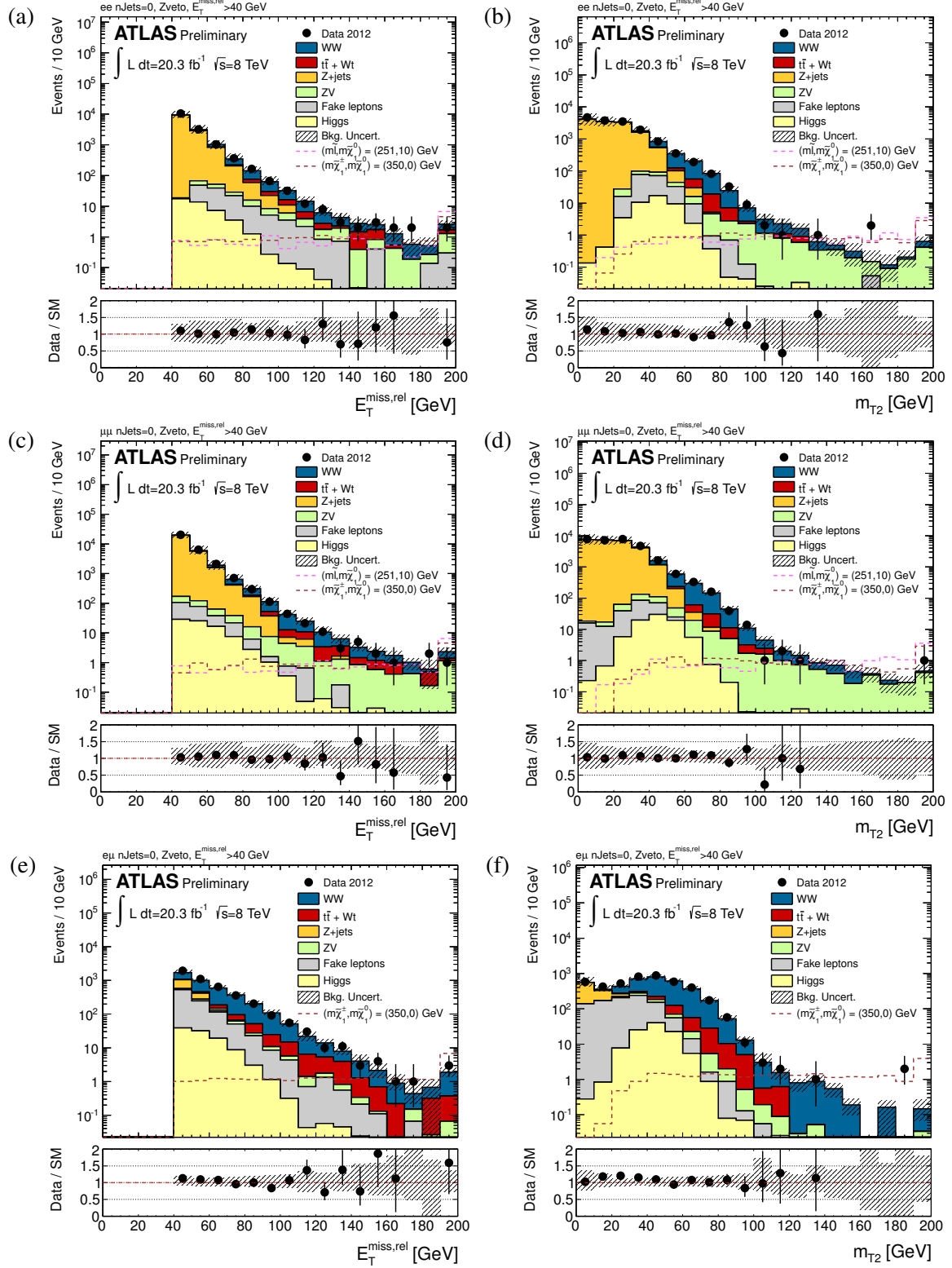
6

Figure 1: Distributions of $E_T^{\text{miss,rel}}$ (left) and m_{T2} (right) in the e^+e^- (top), $\mu^+\mu^-$ (middle) and $e^\pm\mu^\mp$ (bottom) event samples satisfying the event selection of Section 4, as well as $E_T^{\text{miss,rel}} > 40$ GeV, and the Z veto. The expected distributions from the WW, $t\bar{t}$ and ZV processes are corrected with data-driven scale factors obtained in Section 6. The hashed regions represent the total uncertainties on the background estimates. The right-most bin of each plot includes overflow. Illustrative SUSY benchmark models are super-imposed.
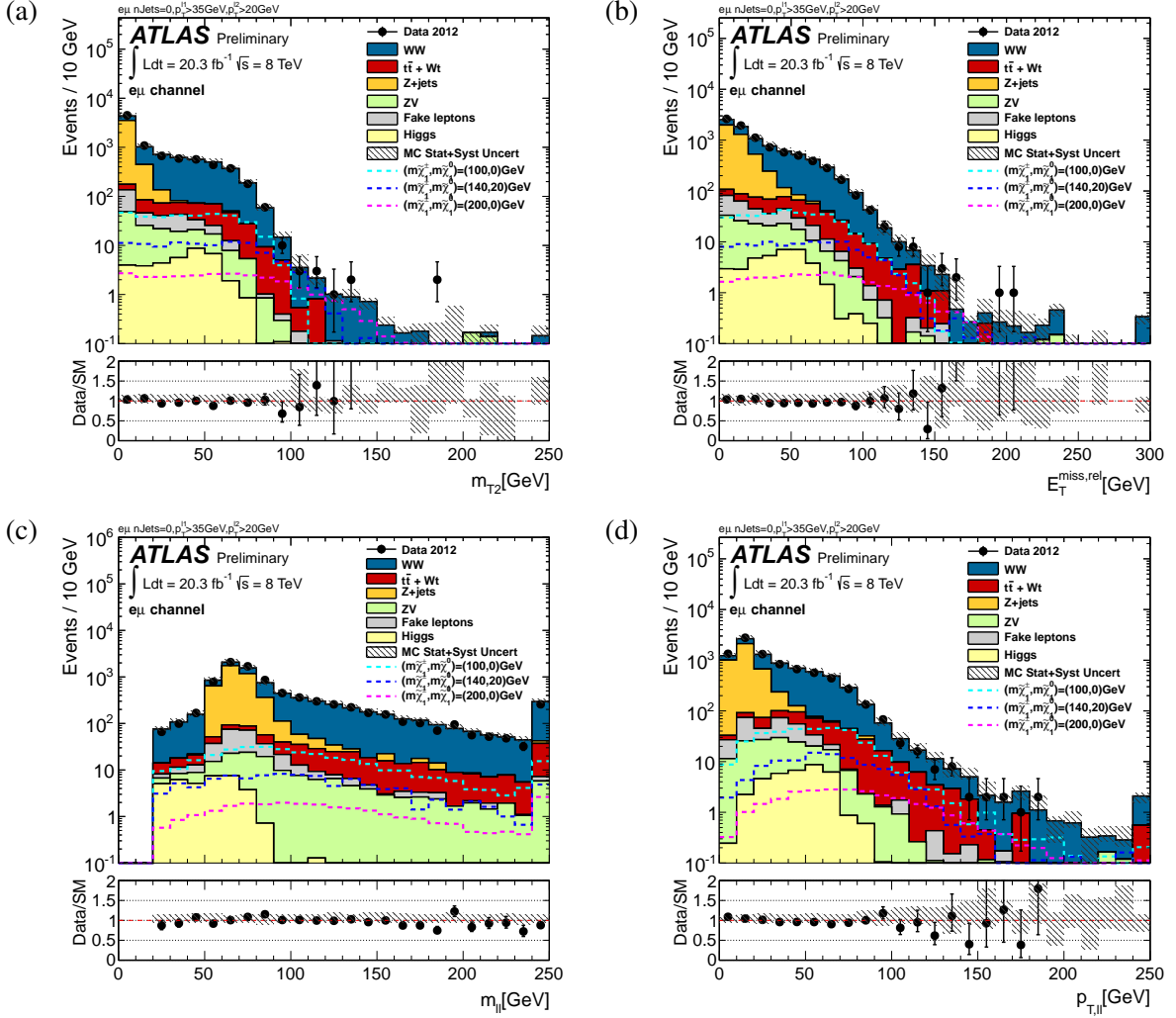
7

Figure 2: Distributions of (a) m_{T2}, (b) $E_T^{miss,rel}$, (c) $m_{\ell\ell}$ and (d) $p_{T,\ell\ell}$ in the $e^{\pm}\mu^{\mp}$ event sample satisfying the event selection of Section 4, as well as $p_T^{\ell 1} > 35$ GeV and $p_T^{\ell 2} > 20$ GeV. The expected distributions from the WW and $t\bar{t}$ processes are corrected with data-driven scale factors obtained in Section 6. The hashed regions represent the total uncertainties on the background estimates. The right-most bin of each plot includes overflow. Illustrative SUSY benchmark models are super-imposed.

6 Standard Model Background Estimation

After requiring two opposite-sign leptons and no jets, the SM background is dominated by events with two leptonically-decaying W bosons coming from WW diboson and top production. Another significant source of background, in the same-flavour channel, is ZV production. The background from Z + jets was found to be negligible in all signal regions.

6.1 WW, top and ZV background estimation

The background contributions from top and WW are estimated by defining dedicated control regions (CR) for each background. Similarly, ZV is estimated by defining control regions in the same-flavour channel. Each control region is dominated by one of the three processes and is designed to be kinemat-

Table 2: Control region definitions of events satisfying the selection of Section 4. 'Z veto' and 'Z select' refer to $|m_{\ell\ell} - m_Z| > 10$ GeV and < 10 GeV, respectively.

SR	SR-$m_{T2,90}$	SR-$m_{T2,110}$	SR-WWa	SR-WWb	SR-WWc
WW CR					
lepton flavour	$e^{\pm}\mu^{\mp}$		$e^{\pm}\mu^{\mp}$		
$m_{\ell\ell}$	Z veto		—		
$\Delta\phi_{\ell\ell}$	—		< 1.8 rad		
$E_T^{\text{miss,rel}}$	> 40 GeV		< 70 GeV	—	
m_{T2}	50–90 GeV		—	< 90 GeV	
Top CR					
b-tagged jets	≥ 1		≥ 1		
signal jets	≥ 2		≥ 1		
lepton flavour	$e^+e^-, \mu^+\mu^-, e^{\pm}\mu^{\mp}$		$e^{\pm}\mu^{\mp}$		
$m_{\ell\ell}$	Z veto		< 80 GeV	< 130 GeV	
$p_{T,\ell\ell}$	—		> 70 GeV	< 170 GeV	< 190 GeV
$\Delta\phi_{\ell\ell}$	—			< 1.8 rad	
$E_T^{\text{miss,rel}}$	> 40 GeV		> 70 GeV	—	
m_{T2}	—		—	> 90 GeV	> 100 GeV
ZV CR					
lepton flavour	$e^+e^-, \mu^+\mu^-$		not defined		
$m_{\ell\ell}$	Z select				
$E_T^{\text{miss,rel}}$	> 40 GeV				
m_{T2}	> 90 GeV	> 110 GeV			

ically as close as possible to a corresponding signal region. Hence each signal region has its own set of two or three control regions; these are defined in Table 2. The simulation is normalised to data in that control region and a normalization factor for the MC is extracted. The simulation and the scale factors are used to obtain the background expectation, N_B^{SR} ($B = WW, t\bar{t}, ZV$) in the signal regions

$$N_B^{\text{SR}} = \left[\frac{N^{\text{CR}} - N_{\text{other}}^{\text{CR}}}{N_{B,\text{MC}}^{\text{CR}}}\right] \times N_{B,\text{MC}}^{\text{SR}},$$

where N^{CR} is the number of events observed in the CR, $N_{\text{other}}^{\text{CR}}$ is the estimated contamination in the CR from sources other than the background considered. The background "scale factor" is defined as $(N^{\text{CR}} - N_{\text{other}}^{\text{CR}})/N_{B,\text{MC}}^{\text{CR}}$, which equals unity if the estimated N_B^{SR} equals the MC prediction. The actual calculation is performed using the combined likelihood fit approach described in Section 6.3.

Contributions from other, less abundant, sources of background are estimated with Monte-Carlo simulation, except for those arising from hadronic jets reconstructed as signal leptons. The latter type of background, referred to as "fake-lepton" background, is estimated using a data-driven method as described in Section 6.2.

The WW control region for SR-m_{T2} is defined by requiring $E_T^{\text{miss,rel}} > 40$ GeV and $50 < m_{T2} < 90$ GeV. The events must also pass the Z veto and contain no jets. Only the $e^{\pm}\mu^{\mp}$ sample is used in this CR because the corresponding regions in the e^+e^- and $\mu^+\mu^-$ samples suffer from contamination from Z/γ^* + jets background. The e^+e^- and $\mu^+\mu^-$ components are therefore evaluated using the $e^{\pm}\mu^{\mp}$ CR, with appropriate ratios of electron and muon efficiencies. The contamination due to non-WW sources in this CR is dominated by the top (13%) and ZV (3%) events, both of which are corrected by the scale factors
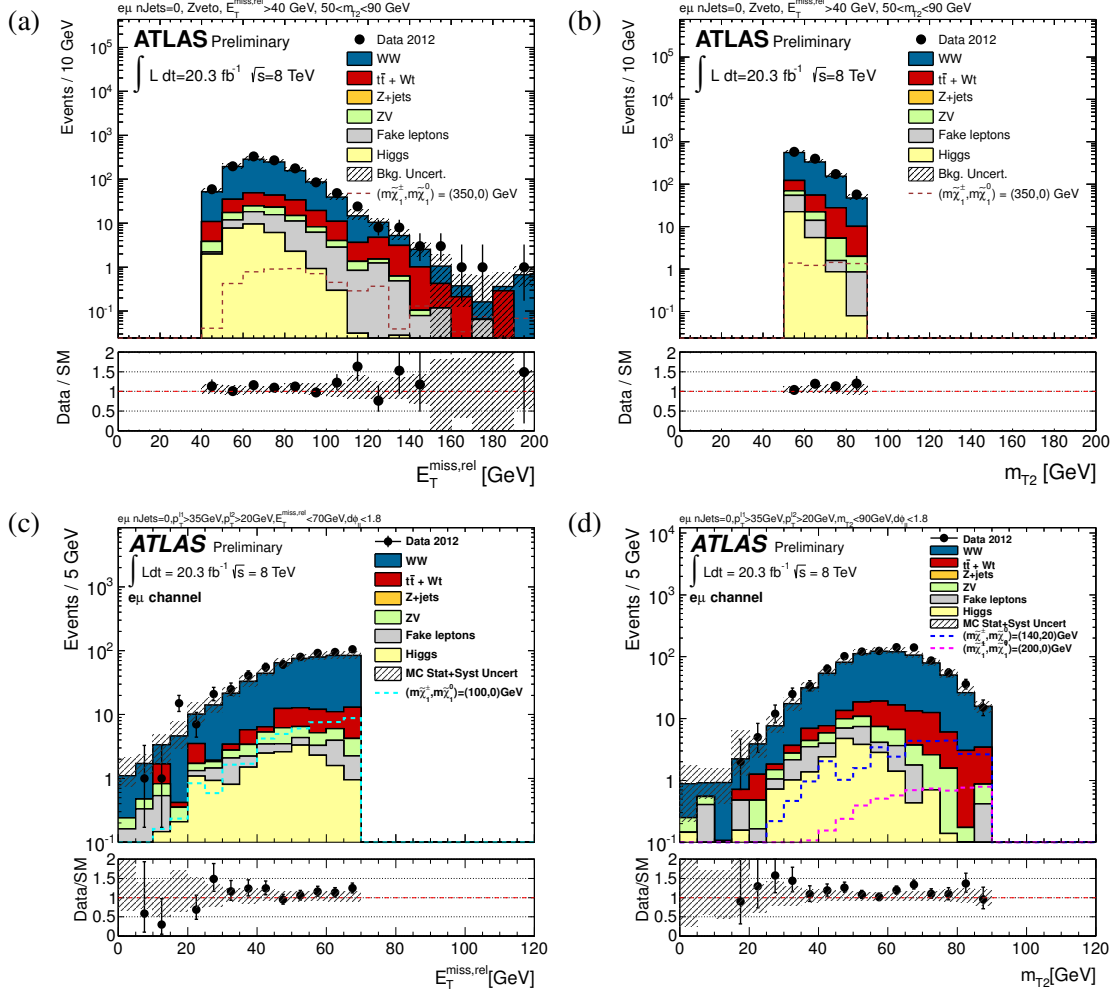
Figure 3: Distributions of (a) $E_T^{miss,rel}$ and (b) m_{T2} in the WW CR for SR-m_{T2}, (c) $E_T^{miss,rel}$ in the WW CR for SR-WWa, and (d) m_{T2} in the WW CR for SR-WWb/c. No data-driven scale factor is applied to the SM distributions. The hashed regions represent the total uncertainties on the background estimates. The right-most bin of (a) includes overflow. Illustrative SUSY benchmark models are super-imposed.

determined from the respective CRs. The scale factor is 1.12 ± 0.14, where the error includes statistical and systematic uncertainties. Details on the systematic errors are provided in Section 7. The scale factor value is consistent with observations in other similar analyses [79]. For SR-WWa, the CR is defined by inverting the $E_T^{miss,rel}$ requirement so that $E_T^{miss,rel} < 70$ GeV, and relaxing the other criteria except for $\Delta\phi_{\ell\ell} < 1.8$ rad. For SR-WWb/c, the m_{T2} cut is inverted to $m_{T2} < 90$ GeV and the $p_{T,\ell\ell}$ and $m_{\ell\ell}$ cuts are removed. The $\Delta\phi_{\ell\ell} < 1.8$ rad cut is still applied. The estimated WW background is larger than the MC prediction by factors of 1.16–1.19 depending on the SR, with total relative uncertainties of 6–8%. Contamination from the signal model $\tilde{\chi}_1^\pm \tilde{\chi}_1^\mp \to W^\pm W^\mp \tilde{\chi}_1^0 \tilde{\chi}_1^0$ with $m_{\tilde{\chi}_1^\pm} > 100$ GeV in this CR is less than 10%. Figure 3 shows the $E_T^{miss,rel}$ and m_{T2} distributions in the WW CRs.

The combined contribution from $t\bar{t}$ and single top events in the signal region is evaluated by normalising MC simulation to data in an appropriate control region. For SR-m_{T2}, the CR is defined using the $e^\pm \mu^\mp$ sample, which suffers from less Z/γ^* + jets background than the $e^+ e^-$ and $\mu^+ \mu^-$ samples, and by requiring at least two signal jets, one of which must be b-tagged. The events must also satisfy $E_T^{miss,rel} > 40$ GeV and the Z veto, but the m_{T2} criteria are not applied. The resulting CR is dominated by
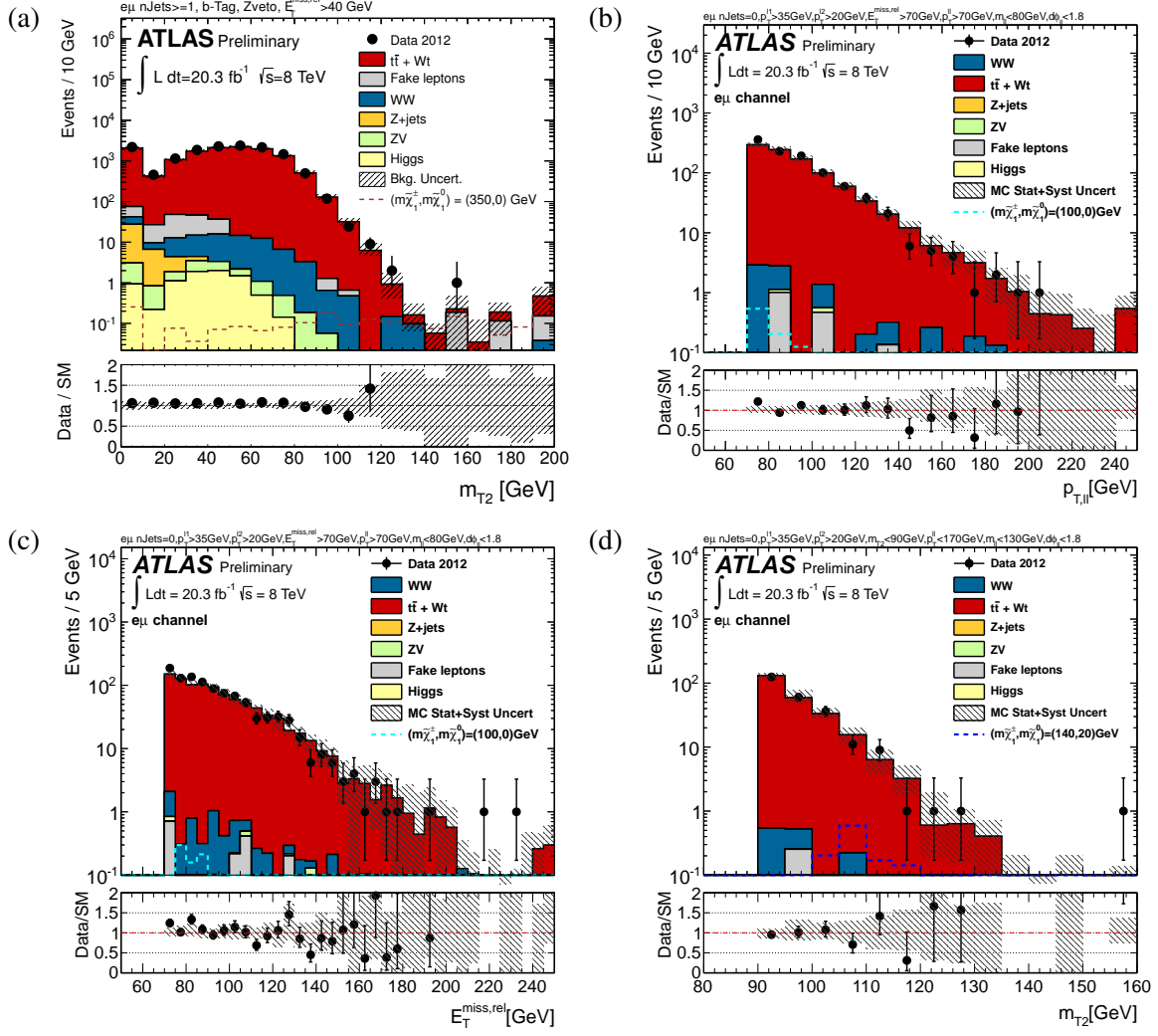
Figure 4: Distributions of (a) m_{T2} in the top CR for SR-m_{T2}, (b) $p_{T,\ell\ell}$ and (c) $E_T^{miss,rel}$ in the top CR for SR-WWa, (d) m_{T2} in the top CR for SR-WWb. No data-driven scale factor is applied to the SM distributions. The hashed regions represent the total uncertainties on the background estimates. The right-most bin of each plot includes overflow. Illustrative SUSY benchmark models are super-imposed.

top events. The contamination from non-top events is about 2% for the $e^{\pm}\mu^{\mp}$ channel. The contamination from SUSY signal is negligible for the models considered. The scale factor is 1.05 ± 0.05 where the error includes systematic uncertainties. For SR-WW, the CRs are defined by requiring at least one b-tagged jet, with all the other criteria unchanged. The contamination from non-top events is 1% or less, and the contamination from SUSY signal is negligible. The scale factors range from 0.98 to 1.07 with total relative uncertainties between 4% and 13%. Figure 4 shows the m_{T2}, $p_{T,\ell\ell}$ and $E_T^{miss,rel}$ distributions in the top CRs.

In the same-flavour channels, the ZV background is significant, and a dedicated CR is designed for its estimation. The CR is defined to be identical to SR-m_{T2} but with the Z veto reversed. The population of data events inside the CR not produced by ZV processes is estimated using data $e\mu$ events inside the Z-window, correcting for the differences between electron and muon reconstruction efficiencies. The estimated ZV background is consistent within statistics with the MC prediction, with scale factors ranging from 0.96 to 1.06 with total relative uncertainties ranging from 15% to 16%. Figure 5 shows the $E_T^{miss,rel}$
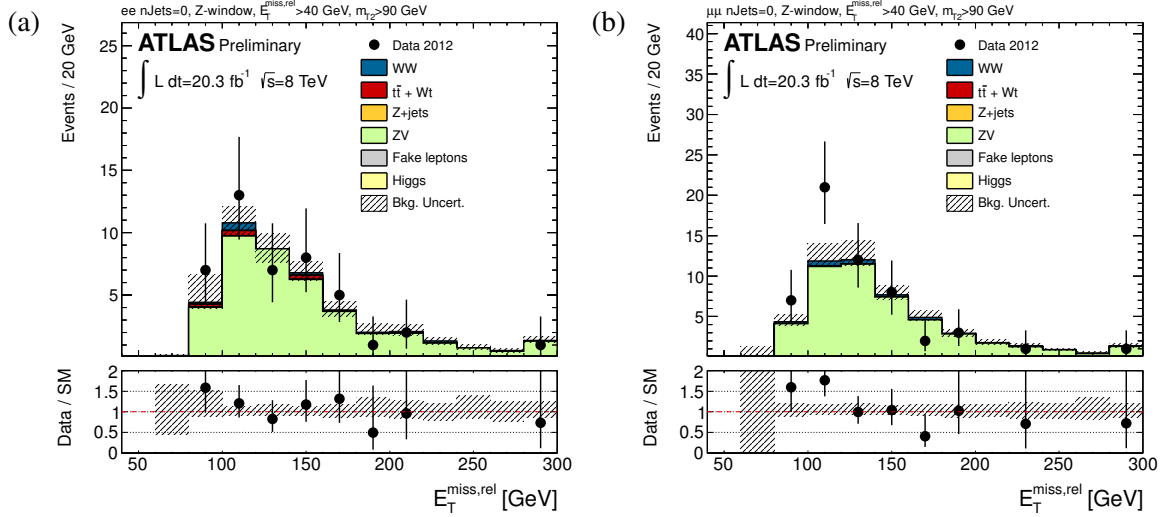
Figure 5: Distributions of $E_T^{\mathrm{miss,rel}}$ in the *ZV* CR for SR-$m_{\mathrm{T2,90}}$ in (a) e^+e^- and (b) $\mu^+\mu^-$ channels. No data-driven scale factor is applied to the SM distributions. The hashed regions represent the total uncertainties on the background estimates. The right-most bin of each plot includes overflow. Illustrative SUSY benchmark models are super-imposed.

distribution in the *ZV* CR.

6.2 Fake lepton background estimation

The term "fake leptons" refers to hadronic jets mistakenly reconstructed as signal leptons or real leptons originating from heavy-flavour decays or photon conversions. The number of fake lepton events is estimated using the "matrix method" [80], which takes advantage of the difference between the candidate and signal leptons defined in Section 4. Recall that the candidate leptons are selected with a looser lepton identification with no isolation requirements. The "real" and "fake" efficiencies are defined as the fraction of real and fake leptons, respectively, that pass the signal-lepton requirements.

The real and fake efficiencies are evaluated in simulated events with $E_T^{\mathrm{miss,rel}} > 40$ GeV using the Monte-Carlo truth information, and corrected for differences between data and MC in separate control samples. The correction for the real efficiency r is derived from $Z \rightarrow \ell\ell$ events. The control sample for the fake efficiency f for misidentified jets or leptons from hadron decays consists of events with two candidate leptons, one b-tagged jet and $E_T^{\mathrm{miss,rel}} < 40$ GeV. One of the two leptons is required to be a muon and to lie within $\Delta R = 0.4$ of the b-tagged jet, and the other lepton is used to measure the fake efficiency. For measuring the fake efficiency for conversions, a $Z + \gamma$ control sample is defined by selecting events with two muons consistent with $Z \rightarrow \mu\mu$, $E_T^{\mathrm{miss,rel}} < 50$ GeV and at least one candidate electron (which is the conversion candidate) with $m_T < 40$ GeV.

The overall f is the weighted average of these two fake efficiencies, according to the relative proportions of each component present in the SR. The number of fake leptons in each SR is obtained by multiplying the observed number of candidate and signal leptons with a 4×4 matrix with terms containing the f and r that relates real and fake leptons to their level of identification. The fake-lepton estimates also include uncertainties related to their dependence on E_T^{miss} and pseudorapidity and as well as uncertainties on the composition of events in each region. The impact of fake-lepton background in the signal regions is very small as shown in Tables 4 and 5.

12

Table 3: Systematic uncertainties (in %) on the total background estimated in SR-m_{T2} and SR-WW. Because of correlations between the systematic uncertainties and the fitted backgrounds, the total uncertainty can be smaller than the quadratic sum of the individual uncertainties.

	SR-$m_{T2,90}$			SR-$m_{T2,110}$			SR-WW ($e^{\pm}\mu^{\mp}$)		
	e^+e^-	$\mu^+\mu^-$	$e^{\pm}\mu^{\mp}$	e^+e^-	$\mu^+\mu^-$	$e^{\pm}\mu^{\mp}$	a	b	c
MC statistics	7.7	6.1	7.5	12	8.2	14	2.9	8.5	11
Jet	9.5	17	12	14	13	6.8	3.1	5.0	7.0
Lepton	3.9	0.5	4.8	5.2	0.5	1.2	1.1	1.7	5.3
Soft term	1.9	3.2	6.0	3.0	1.0	0.7	1.0	4.6	4.3
b-tagging	0.2	0.2	0.2	0.2	0.3	0.2	0.4	0.7	0.5
Fake lepton	1.0	0.7	0.6	1.5	1.9	3.0	0.1	1.2	1.2
Luminosity	0.0	0.0	0.0	0.0	0.0	0.0	0.1	0.1	0.1
Theory & modelling	9.7	9.4	11	32	36	43	12	14	14
Total	14	15	16	36	38	45	12	17	20

6.3 Fitting procedure

For each signal region, a simultaneous likelihood fit [81] to the signal regions and the control regions is performed to normalise the top, WW and ZV (in the case of SR-m_{T2} only) background estimates and to determine or limit a potential signal contribution. The inputs to the fit are:

- For each control region, the observed number of events in the top, WW and ZV and the expected background estimate from simulation.

- The expected background in the signal regions for all processes determined from simulation.

- The fake-lepton background estimate in the signal regions as described in Section 6.2.

The event count in each control and signal region is treated with a Poisson probability density function. The systematic uncertainties on the expected background yields are included as nuisance parameters, constrained to be Gaussian with a width determined from the size of the uncertainty. Correlations in the nuisance parameters between the control and signal regions, and background processes are taken into account. The Poisson probability density function also includes free parameters to scale the expected contribution from top, WW and, where relevant, ZV in the control regions. A likelihood is formed as the product of these probability density functions and the constraints on the nuisance parameters. The free parameters and the nuisance parameters are adjusted to maximise the likelihood.

7 Systematic Uncertainties

Systematics uncertainties have an impact on the estimates of the backgrounds and signal event yields in the control and signal regions. The relative sizes of these sources of systematic uncertainty in SR-m_{T2} and SR-WW are detailed in Table 3.

The 'MC statistics' uncertainties arise from the limited number of simulated events in the signal and control regions. The largest contributions are due to the simulated background samples in the signal regions.

The dominant experimental systematic uncertainties, labelled 'jet' in Table 3, come from the propagation of the jet energy scale calibration [82–87] and resolution [88] uncertainties. The 'lepton' uncertainties include lepton reconstruction, identification and trigger efficiencies, as well as lepton energy and momentum measurements [71, 89–91]. Jet and lepton energy scale uncertainties are propagated to the

$E_{\mathrm{T}}^{\mathrm{miss}}$ evaluation. An additional 'soft term' uncertainty is associated with energy deposits not assigned to any reconstructed objects. The 'b-tagging' row refers to the uncertainties on the b-jet identification efficiency and charm and light-flavour jet rejection factors [92]. The 'fake lepton' uncertainties arise from the data-driven estimates of the fake-lepton background described in Section 6.2. The dominant sources are $E_{\mathrm{T}}^{\mathrm{miss,rel}}$ and η dependences of the fake rates, difference between the light and heavy flavour jets, and the statistics of the control samples. The uncertainty on the integrated luminosity is ±2.8%. It is derived, following the same methodology as that detailed in Ref. [93], from a preliminary calibration of the luminosity scale derived from beam-separation scans performed in November 2012.

Generator modelling uncertainties are obtained by comparing the results from POWHEG plus HERWIG to MC@NLO generators for top events, and POWHEG to SHERPA for diboson events. Parton showering uncertainties are extracted in top events by comparing POWHEG plus HERWIG with POWHEG plus PYTHIA. Special $t\bar{t}$ samples are generated using AcerMC with PYTHIA to evaluate the uncertainties related to the amount of initial and final-state radiation. The effects of all these uncertainties are summarised in the "theory & modelling" field of Table 3. The dominant contribution comes from the difference between POWHEG and SHERPA for diboson production.

Signal cross sections are calculated to NLO in the strong coupling constant. Their uncertainties are taken from an envelope of cross section predictions using different PDF sets and factorisation and renormalisation scales, as described in Ref. [94].

8   Results

Figures 6 and 7 show the comparison between data and the SM prediction for key kinematical variables in different signal regions. Tables 4 and 5 compare the observed yields in each signal region with those predicted for the SM background. Good agreement is observed across all channels.

Limits are set on the visible cross-section for possible non-SM processes in each channel, $\sigma_{\mathrm{vis}} = \sigma \cdot \epsilon \cdot A$, where A and ϵ are the analysis acceptance and efficiency, respectively. Upper limits are calculated at 95% confidence level (CL) using the modified frequentist $\mathrm{CL_s}$ prescription [95] by comparing the number of observed events in data with the SM expectation using the profile likelihood ratio as test statistic. All systematic uncertainties and their correlations are taken into account via nuisance parameters.

9   Interpretation

In the absence of an excess over the SM background expectations, 95% confidence-level exclusion limits are set on the slepton, chargino and neutralino masses within the specific scenarios considered. Since the SRs are not mutually exclusive, the SR with the best expected exclusion limit is chosen for each model point.

Direct slepton scenario   Figure 8 shows 95% CL exclusion regions for the direct production of right-handed (a), left-handed (b), and both right- and left-handed (c) selectrons and smuons of equal mass in the $m_{\tilde{\chi}_1^0}$–$m_{\tilde{\ell}}$ plane obtained from the e^+e^- and $\mu^+\mu^-$ channels of SR-$m_{\mathrm{T2},90}$ and SR-$m_{\mathrm{T2},110}$. Each plot shows the 95% $\mathrm{CL_s}$ expected (dashed black) and observed (solid red) limits, including all uncertainties except the theoretical uncertainty on the signal cross section. The solid yellow band indicates the impact of experimental uncertainties on the expected limits whereas the dashed red lines around the observed limit show the changes in the observed limit as the signal cross-sections are scaled up and down by the 1σ theoretical uncertainties. A common value for left and right-handed selectron and smuon mass between 90 GeV and 320 GeV is excluded for a massless neutralino, where these numbers correspond to the observed value minus the signal theoretical uncertainty. The sensitivity decreases as the value of
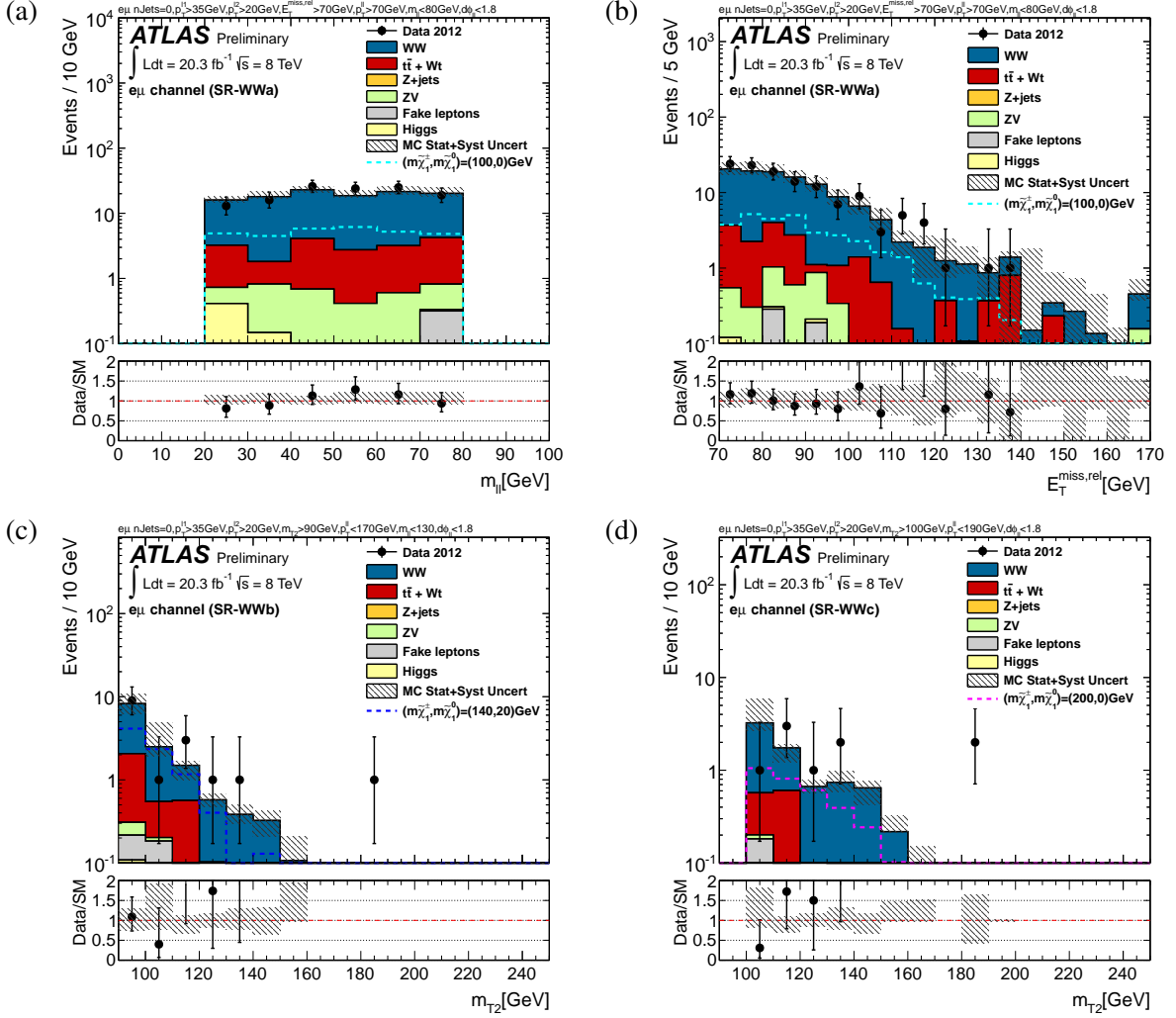
14

Figure 6: Distributions of (a) $m_{\ell\ell}$ and (b) $E_T^{\mathrm{miss,rel}}$ in SR-WWa, and m_{T2} in (c) SR-WWb and (d) SR-WWc. The expected distributions from the WW and $t\bar{t}$ processes are corrected with data-driven scale factors obtained in Section 6. The hashed regions represent the sum of systematic and statistical uncertainties arising from limited numbers of MC events. The effect of limited data events in the CR is included in the systematic uncertainty. The component ZV includes the contributions from WZ and ZZ events. All statistical uncertainties are added in quadrature whereas the systematic uncertainties are obtained after taking full account of all correlations between sources, backgrounds and channels. The right-most bin of (b) includes overflow. Illustrative SUSY benchmark models are super-imposed.

$m_{\tilde{\ell}} - m_{\tilde{\chi}_1^0}$ decreases, which in turn lowers the m_{T2} end point towards that of the SM backgrounds. For a 100 GeV neutralino, sleptons with masses between 160 GeV and 320 GeV are excluded. The present result cannot be directly compared with the previous ATLAS slepton limits in Ref. [35] which used a flavour-blind signal region and searched for a single-slepton flavour with both right-handed and left-handed contributions.

Chargino-to-slepton scenario The direct $\tilde{\chi}_1^\pm$ pair production limits are set for the simplified model. The resulting limit for $\tilde{\chi}_1^\pm\tilde{\chi}_1^\mp$ production is illustrated in Fig. 8 (d). Chargino masses between 130 GeV and 450 GeV are excluded at 95% CL for a 20 GeV neutralino.
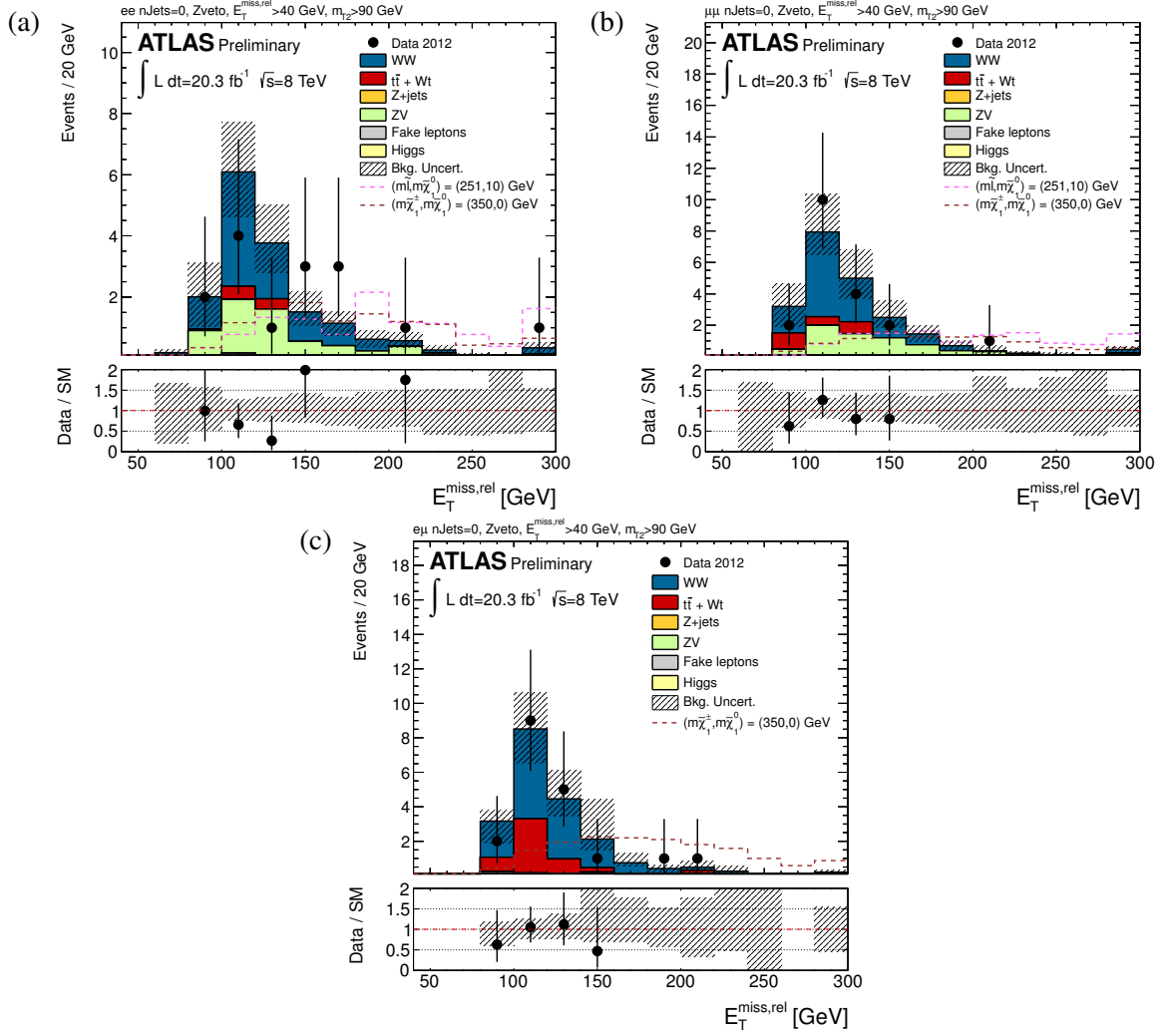
Figure 7: Distributions of $E_T^{\mathrm{miss,rel}}$ in the di-electron (a), di-muon (b), electron-muon (c) in SR-$m_{\mathrm{T2,90}}$. The expected distributions from the WW, $t\bar{t}$ and ZV processes are corrected with data-driven scale factors obtained in Section 6. The hashed regions represent the sum of systematic and statistical uncertainties arising from limited numbers of MC events. The effect of limited data events in the CR is included in the systematic uncertainty. The component ZV includes the contributions from WZ and ZZ events. All statistical uncertainties are added in quadrature whereas the systematic uncertainties are obtained after taking full account of all correlations between sources, backgrounds and channels. The right-most bin of each plot includes overflow. Illustrative SUSY benchmark models are super-imposed.

Chargino-to-W scenario The 95% CL limits on the cross-section with respect to the simplified-model cross-section with bino-like $\tilde{\chi}_1^0$ and wino-like $\tilde{\chi}_1^\pm$ are presented in the $m_{\tilde{\chi}_1^\pm}$–$m_{\tilde{\chi}_1^0}$ plane in Figure 9 (a) and (b) for the signal region best contributing to the limit. The most sensitive region is $140 \leq m_{\tilde{\chi}_1^\pm} \leq 210\,\mathrm{GeV}$ and $0 \leq m_{LSP} \leq 40\,\mathrm{GeV}$ where an average observed (expected) 95% CL exclusion limit for $\sigma/\sigma_{\mathrm{SUSY}}$ of 2.5 (2.0) is obtained. In this region, the $\tilde{\chi}_1^\pm$ cross section is still high (0.3–1.2 pb) and the W bosons are boosted and therefore distinguishable from the WW background. Figure 9 (c) shows the observed and expected 95% CL$_{\mathrm{s}}$ upper limits on the cross section as a function of $m_{\tilde{\chi}_1^\pm}$ for a massless $\tilde{\chi}_1^0$, normalised to the model cross-section. The SRs with the smallest expected exclusion cross-section are SR-WWa for $m_{\tilde{\chi}_1^\pm} = 100\,\mathrm{GeV}$, SR-$WW$b for 110–160 GeV and SR-WWc for 170–250 GeV. The

16

Table 4: Observed and expected numbers of events in regions SR-$m_{T2,90}$ and SR-$m_{T2,110}$ separated by lepton flavour. The first two rows of the signal expectation are direct slepton production with degenerate left- and right-handed sleptons masses, and the last two rows are chargino production with intermediate sleptons and sneutrinos. Also shown are the observed and expected 95% CL upper limits on the visible cross-section, $\sigma_{\mathrm{vis}}^{95}$, for non-SM events.

SR-$m_{T2,90}$	e^+e^-	$e^\pm\mu^\mp$	$\mu^+\mu^-$	all
Observed	15	19	19	53
Background total	16.6 ± 2.3	20.7 ± 3.2	22.4 ± 3.3	59.7 ± 7.3
$\quad WW$	9.3 ± 1.6	14.1 ± 2.2	12.6 ± 2.0	36.1 ± 5.1
$\quad ZV$ ($V = W$ or Z)	6.3 ± 1.5	0.8 ± 0.3	7.3 ± 1.7	14.4 ± 3.2
$\quad$Top	$0.9^{+1.1}_{-0.9}$	5.6 ± 2.1	2.5 ± 1.8	8.9 ± 3.9
$\quad$Higgs	0.11 ± 0.04	0.19 ± 0.05	0.08 ± 0.04	0.38 ± 0.08
$\quad$Fake	$0.00^{+0.18}_{-0.00}$	$0.00^{+0.14}_{-0.00}$	$0.00^{+0.15}_{-0.00}$	$0.00^{+0.28}_{-0.00}$
Signal expectation				
$(m_{\tilde{\ell}}, m_{\tilde{\chi}_1^0}) = (191, 90)$ GeV	21.6	0	21.6	43.2
$(m_{\tilde{\ell}}, m_{\tilde{\chi}_1^0}) = (251, 10)$ GeV	12.2	0	12.5	24.7
$(m_{\tilde{\chi}_1^\pm}, m_{\tilde{\chi}_1^0}) = (350, 0)$ GeV	11.7	16.6	10.5	38.8
$(m_{\tilde{\chi}_1^\pm}, m_{\tilde{\chi}_1^0}) = (425, 75)$ GeV	4.3	6.7	4.4	15.4
Observed $\sigma_{\mathrm{vis}}^{95}$ (fb)	0.44	0.51	0.47	0.81
Expected $\sigma_{\mathrm{vis}}^{95}$ (fb)	$0.50^{+0.22}_{-0.15}$	$0.57^{+0.25}_{-0.17}$	$0.58^{+0.25}_{-0.17}$	$1.00^{+0.41}_{-0.28}$
SR-$m_{T2,110}$	e^+e^-	$e^\pm\mu^\mp$	$\mu^+\mu^-$	all
Observed	4	5	4	13
Background total	6.1 ± 2.2	4.4 ± 2.0	6.3 ± 2.4	16.9 ± 6.0
$\quad WW$	2.7 ± 1.5	3.6 ± 2.0	2.9 ± 1.6	9.1 ± 4.9
$\quad ZV$ ($V = W$ or Z)	2.7 ± 1.4	0.2 ± 0.1	3.4 ± 1.8	6.3 ± 3.3
$\quad$Top	0.7 ± 0.7	0.6 ± 0.4	0.0 ± 0.0	1.3 ± 1.0
$\quad$Higgs	0.05 ± 0.03	0.12 ± 0.04	0.05 ± 0.02	0.22 ± 0.05
$\quad$Fake	$0.00^{+0.09}_{-0.00}$	$0.00^{+0.13}_{-0.00}$	$0.00^{+0.12}_{-0.00}$	$0.00^{+0.28}_{-0.00}$
Signal expectation				
$(m_{\tilde{\ell}}, m_{\tilde{\chi}_1^0}) = (191, 90)$ GeV	12.3	0	12.0	24.3
$(m_{\tilde{\ell}}, m_{\tilde{\chi}_1^0}) = (251, 10)$ GeV	10.5	0	11.2	21.7
$(m_{\tilde{\chi}_1^\pm}, m_{\tilde{\chi}_1^0}) = (350, 0)$ GeV	9.5	14.0	8.7	32.2
$(m_{\tilde{\chi}_1^\pm}, m_{\tilde{\chi}_1^0}) = (425, 75)$ GeV	3.7	1.1	3.8	8.5
Observed $\sigma_{\mathrm{vis}}^{95}$ (fb)	0.27	0.35	0.28	0.54
Expected $\sigma_{\mathrm{vis}}^{95}$ (fb)	$0.33^{+0.16}_{-0.10}$	$0.33^{+0.16}_{-0.09}$	$0.33^{+0.16}_{-0.10}$	$0.62^{+0.23}_{-0.16}$

excluded cross-section is above the model cross-section by a factor 1.9–2.8 in the range 100–190 GeV and then degrades gradually to 4.7 when reaching a $\tilde{\chi}_1^\pm$ mass of 250 GeV. The best sensitivity is obtained for the $(m_{\tilde{\chi}_1^\pm}, m_{\tilde{\chi}_1^0}) = (100, 0)$ GeV mass point where $\sigma/\sigma_{\mathrm{SUSY}} = 1.79$.

GMSB model point The CL$_s$ value is also calculated for the GMSB model point where the chargino is the NLSP [$m(\tilde{\chi}_1^\pm) = 110$ GeV, $m(\tilde{\chi}_1^0) = 113$ GeV and $m(\tilde{\chi}_2^0) = 130$ GeV] [40]. The observed CL$_s$ value is found to be 0.52 using the SR-WWa region, which the most sensitive signal region for this point. The expected and observed 95% CL limit on $\sigma/\sigma_{\mathrm{SUSY}}$ are 2.6 and 2.9, respectively.

Table 5: Observed and expected numbers of events in SR-*WW*a, b and c. The first three rows of the signal expectation are simplified models, and the last row is the GMSB model of Ref. [40]. Also shown are the observed and expected 95% CL upper limits on the visible cross-section, $\sigma_{\mathrm{vis}}^{95}$, for non-SM events. N/A means not applicable.

	SR-*WW*a	SR-*WW*b	SR-*WW*c
Observed	123	16	9
Background total	117.9 ± 14.6	13.6 ± 2.3	7.4 ± 1.5
Top	15.2 ± 6.6	2.7 ± 1.1	1.0 ± 0.7
WW	98.6 ± 14.6	10.2 ± 2.1	5.9 ± 1.3
ZV ($V = W$ or Z)	3.4 ± 0.8	$0.26^{+0.31}_{-0.26}$	0.29 ± 0.14
Higgs	0.76 ± 0.14	0.21 ± 0.06	0.10 ± 0.04
fake	$0.02^{+0.33}_{-0.02}$	$0.26^{+0.30}_{-0.26}$	$0.12^{+0.17}_{-0.12}$
Signal expectation			
$(m_{\tilde{\chi}_1^\pm}, m_{\tilde{\chi}_1^0}) = (100, 0)$ GeV	31	N/A	N/A
$(m_{\tilde{\chi}_1^\pm}, m_{\tilde{\chi}_1^0}) = (140, 20)$ GeV	N/A	8.2	N/A
$(m_{\tilde{\chi}_1^\pm}, m_{\tilde{\chi}_1^0}) = (200, 0)$ GeV	N/A	N/A	3.3
$(m_{\tilde{\chi}_1^\pm}, m_{\tilde{\chi}_1^0}) = (110, 113)$ GeV	18	4.3	N/A
Observed $\sigma_{\mathrm{vis}}^{95}$ (fb)	1.94	0.58	0.43
Expected $\sigma_{\mathrm{vis}}^{95}$ (fb)	$1.77^{+0.66}_{-0.49}$	$0.51^{+0.21}_{-0.15}$	$0.37^{+0.18}_{-0.11}$

10 Summary

This note presented searches for slepton and chargino pair production in final states with two leptons, missing transverse momentum, and no jets performed using 20.3 fb^{-1} of proton-proton collision data at $\sqrt{s} = 8$ TeV recorded with the ATLAS experiment at the Large Hadron Collider.

No significant excesses over the Standard Model predictions are observed. In scenarios where sleptons decay directly into the lightest neutralino and a charged lepton, a common value for left and right-handed slepton masses between 90 GeV and 320 GeV is excluded at 95% confidence level for a massless neutralino. In the scenario of chargino pair production, with wino-like charginos decaying into the lightest neutralino via an intermediate slepton, chargino masses between 130 GeV and 450 GeV are excluded at 95% confidence level for a 20 GeV neutralino. In the scenario of chargino pair production followed by the $\tilde{\chi}_1^\pm \rightarrow W^\pm \tilde{\chi}_1^0$ decay, the excluded cross-section is above the model cross-section by a factor 1.9–2.8 in the $\tilde{\chi}_1^\pm$ mass range 100–190 GeV and then degrades gradually to 4.7 when reaching a $\tilde{\chi}_1^\pm$ mass of 250 GeV. Best sensitivity is obtained for the $(m_{\tilde{\chi}_1^\pm}, m_{\tilde{\chi}_1^0}) = (100, 0)$ GeV mass point where $\sigma / \sigma_{\mathrm{SUSY}} = 1.8$ In the case of the GMSB model point, the observed 95% CL limit on $\sigma / \sigma_{\mathrm{SUSY}}$ is 2.9.

References

[1] H. Miyazawa, *Baryon Number Changing Currents*, Prog. Theor. Phys. **36 (6)** (1966) 1266–1276.

[2] P. Ramond, *Dual Theory for Free Fermions*, Phys. Rev. **D3** (1971) 2415–2418.

[3] Y. A. Gol'fand and E. P. Likhtman, *Extension of the Algebra of Poincare Group Generators and Violation of p Invariance*, JETP Lett. **13** (1971) 323–326. [Pisma Zh. Eksp. Teor. Fiz. **13** (1971) 452–455].

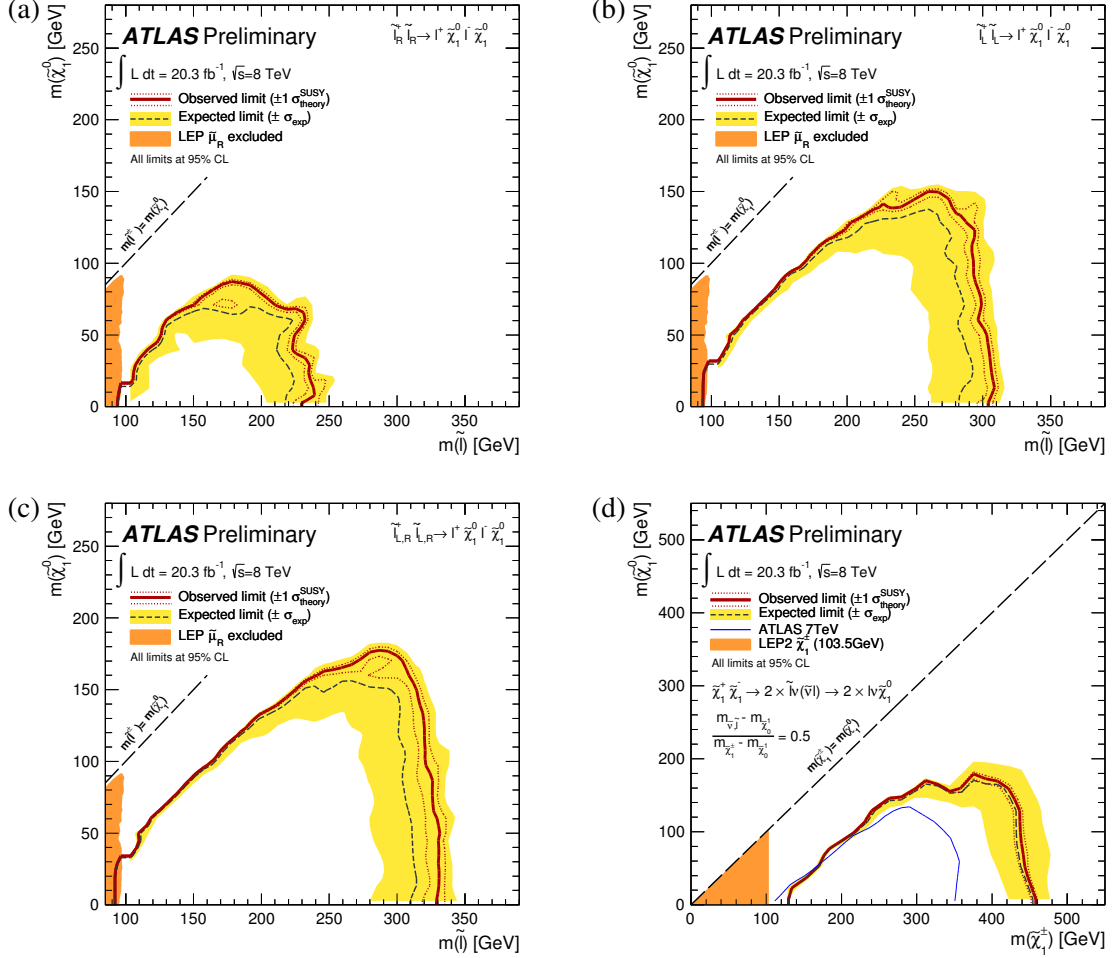[4] A. Neveu and J. H. Schwarz, *Factorizable dual model of pions*, Nucl. Phys. **B31** (1971) 86–112.

Figure 8: 95% CL exclusion limits for (a) right-handed, (b) left-handed, and (c) both right- and left-handed (mass degenerate) selectron and smuon production in the $m_{\tilde{\chi}_1^0}$–$m_{\tilde{\ell}}$ plane. (d) 95% CL exclusion limits for $\tilde{\chi}_1^\pm \tilde{\chi}_1^\mp$ pair production in the simplified model with sleptons and sneutrinos with $m_{\tilde{\ell}} = m_{\tilde{\nu}} = (m_{\tilde{\chi}_1^\pm} + m_{\tilde{\chi}_1^0})/2$. The dashed and solid lines show the 95% CL$_s$ expected and observed limits, respectively, including all uncertainties except for the theoretical signal cross-section uncertainty (PDF and scale). The solid band around the expected limit shows the $\pm 1\sigma$ result where all uncertainties, except those on the signal cross-sections, are considered. The $\pm 1\sigma$ lines around the observed limit represent the results obtained when moving the nominal signal cross-section up or down by the $\pm 1\sigma$ theoretical uncertainty. Illustrated also are the LEP limits [38] on the mass of the right-handed smuon $\tilde{\mu}_R$ in (a)–(c), and on the mass of the chargino in (d). The blue line in (d) indicates the limit from the previous analysis with the 7 TeV data [35].

[5] A. Neveu and J. H. Schwarz, *Quark Model of Dual Pions*, Phys. Rev. **D4** (1971) 1109–1111.

[6] J. Gervais and B. Sakita, *Field theory interpretation of supergauges in dual models*, Nucl. Phys. **B34** (1971) 632–639.

[7] D. V. Volkov and V. P. Akulov, *Is the Neutrino a Goldstone Particle?*, Phys. Lett. **B46** (1973) 109–110.
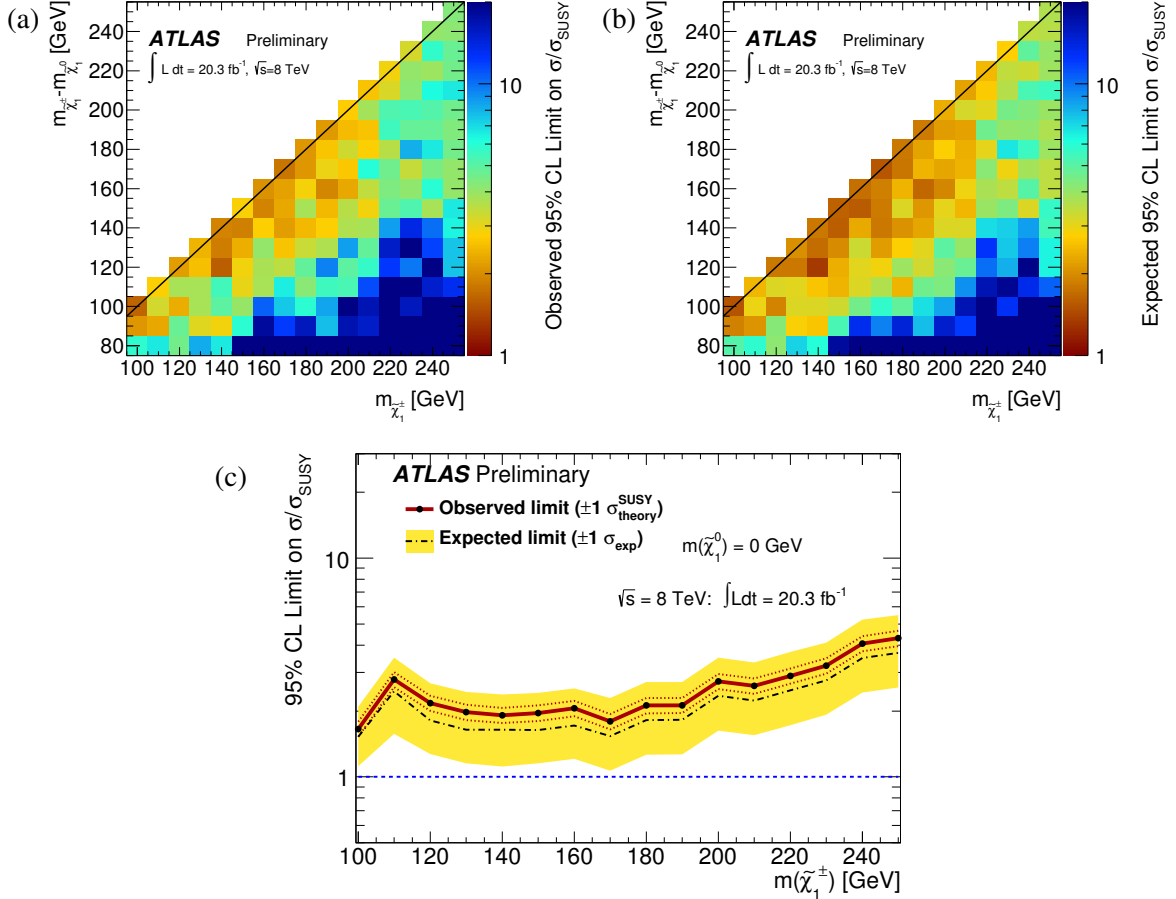
Figure 9: Observed (a) and expected (b) 95% CLs upper limits of the cross-section obtained from SR-*WW*a–c for simplified models with bino-like $\tilde{\chi}_1^0$ and wino-like $\tilde{\chi}_1^\pm$ in the $m_{\tilde{\chi}_1^0}$–$m_{\tilde{\chi}_1^\pm}$ plane. (c) Observed and expected 95% CLs upper limits of the cross-section as a function of $m_{\tilde{\chi}_1^\pm}$ for massless $\tilde{\chi}_1^0$ normalised to the simplified-model cross-section.

[8] J. Wess and B. Zumino, *A Lagrangian Model Invariant Under Supergauge Transformations*, Phys. Lett. **B49** (1974) 52.

[9] J. Wess and B. Zumino, *Supergauge Transformations in Four-Dimensions*, Nucl. Phys. **B70** (1974) 39–50.

[10] S. Weinberg, *Implications of Dynamical Symmetry Breaking*, Phys. Rev. **D13** (1976) 974–996.

[11] E. Gildener, *Gauge Symmetry Hierarchies*, Phys. Rev. **D14** (1976) 1667.

[12] S. Weinberg, *Implications of Dynamical Symmetry Breaking: An Addendum*, Phys. Rev. **D19** (1979) 1277–1280.

[13] L. Susskind, *Dynamics of Spontaneous Symmetry Breaking in the Weinberg- Salam Theory*, Phys. Rev. **D20** (1979) 2619–2625.

[14] P. Fayet, *Supersymmetry and Weak, Electromagnetic and Strong Interactions*, Phys. Lett. **B64** (1976) 159.

[15] P. Fayet, *Spontaneously Broken Supersymmetric Theories of Weak, Electromagnetic and Strong Interactions*, Phys. Lett. **B69** (1977) 489.

[16] G. R. Farrar and P. Fayet, *Phenomenology of the Production, Decay, and Detection of New Hadronic States Associated with Supersymmetry*, Phys. Lett. **B76** (1978) 575–579.

[17] P. Fayet, *Relations Between the Masses of the Superpartners of Leptons and Quarks, the Goldstino Couplings and the Neutral Currents*, Phys. Lett. **B84** (1979) 416.

[18] S. Dimopoulos and H. Georgi, *Softly Broken Supersymmetry and SU(5)*, Nucl. Phys. **B193** (1981) 150.

[19] L. Evans and P. Bryant, *LHC Machine*, JINST **3** (2008) S08001.

[20] A. Djouadi, J.-L. Kneur, and G. Moultaka, *SuSpect: A Fortran code for the supersymmetric and Higgs particle spectrum in MSSM*, Comput. Phys. Commun. **176** (2007) 426–455, `arXiv:hep-ph/0211331`.

[21] C. F. Berger, J. S. Gainer, J. L. Hewett, and T. G. Rizzo, *Supersymmetry Without Prejudice*, JHEP **0902** (2009) 023, `arXiv:hep-ph/0211331`.

[22] S. S. AbdusSalam et al., *Fitting the Phenomenological MSSM*, Phys. Rev. **D81** (2010) 095012, `arXiv:0904.2548 [hep-ph]`.

[23] R. Barbieri and G. F. Giudice, *Upper Bounds on Supersymmetric Particle Masses*, Nucl. Phys. **B306** (1988) 63.

[24] B. de Carlos and J. A. Casas, *One loop analysis of the electroweak breaking in supersymmetric models and the fine tuning problem*, Phys. Lett. **B309** (1993) 320–328, `arXiv:hep-ph/9303291`.

[25] M. Dine and W. Fischler, *A Phenomenological Model of Particle Physics Based on Supersymmetry*, Phys. Lett. **B110** (1982) 227.

[26] L. Alvarez-Gaume, M. Claudson, and M. B. Wise, *Low-Energy Supersymmetry*, Nucl. Phys. **B207** (1982) 96.

[27] C. R. Nappi and B. A. Ovrut, *Supersymmetric Extension of the SU(3) x SU(2) x U(1) Model*, Phys. Lett. **B113** (1982) 175.

[28] M. Dine and A. E. Nelson, *Dynamical supersymmetry breaking at low-energies*, Phys. Rev. **D48** (1993) 1277–1287, `arXiv:hep-ph/9303230`.

[29] M. Dine, A. E. Nelson, and Y. Shirman, *Low-energy dynamical supersymmetry breaking simplified*, Phys. Rev. **D51** (1995) 1362–1370, `arXiv:hep-ph/9408384`.

[30] M. Dine, A. E. Nelson, Y. Nir, and Y. Shirman, *New tools for low-energy dynamical supersymmetry breaking*, Phys. Rev. **D53** (1996) 2658–2669, `arXiv:hep-ph/9507378`.

[31] L. Randall and R. Sundrum, *Out of this world supersymmetry breaking*, Nucl. Phys. **B557** (1999) 79–118, `arXiv:hep-th/9810155 [hep-th]`.

[32] G. F. Giudice, M. A. Luty, H. Murayama, and R. Rattazzi, *Gaugino mass without singlets*, JHEP **9812** (1998) 027, `arXiv:hep-ph/9810442 [hep-ph]`.

[33] G. Belanger, F. Boudjema, A. Cottrant, A. Pukhov, and A. Semenov, *WMAP constraints on SUGRA models with non-universal gaugino masses and prospects for direct detection*, Nucl. Phys. **B706** (2005) 411–454, `arXiv:hep-ph/0407218` [hep-ph].

[34] S. King, J. Roberts, and D. Roy, *Natural dark matter in SUSY GUTs with non-universal gaugino masses*, JHEP **0710** (2007) 106, `arXiv:0705.4219` [hep-ph].

[35] ATLAS Collaboration, *Search for direct slepton and gaugino production in final states with two leptons and missing transverse momentum with the ATLAS detector in pp collisions at $\sqrt{s} = 7$ TeV*, Phys. Lett. **B718** (2013) 879–901, `arXiv:1208.2884` [hep-ex].

[36] CMS Collaboration, *Search for direct EWK production of SUSY particles in multilepton modes with 8 TeV data*, CMS-PAS-SUS-12-022, `http://cds.cern.ch/record/1496092`.

[37] ATLAS Collaboration, *Search for direct slepton and gaugino production in final states with hadronic taus and missing transverse momentum with the ATLAS detector in pp collisions at $\sqrt{s} = 8$ TeV*, ATLAS-CONF-2013-028, `https://cds.cern.ch/record/1525889`.

[38] LEP SUSY Working Group (ALEPH, DELPHI, L3, OPAL), Notes LEPSUSYWG/01-03.1, 04-01.1, http://lepsusy.web.cern.ch/lepsusy/Welcome.html.

[39] H. Baer, C.-h. Chen, F. Paige, and X. Tata, *Detecting Sleptons at Hadron Colliders and Supercolliders*, Phys. Rev. **D49** (1994) 3283–3290, `arXiv:hep-ph/9311248`.

[40] D. Curtin, P. Jaiswal, and P. Meade, *Charginos Hiding In Plain Sight*, `arXiv:1206.6888` [hep-ph].

[41] ATLAS Collaboration, *The ATLAS Experiment at the CERN Large Hadron Collider*, JINST **3** (2008) S08003.

[42] GEANT4 Collaboration, S. Agostinelli et al., *GEANT4: A simulation toolkit*, Nucl. Instrum. Meth. **A506** (2003) 250–303.

[43] ATLAS Collaboration, *The ATLAS Simulation Infrastructure*, Eur. Phys. J. **C70** (2010) 823–874, `arXiv:1005.4568` [physics.ins-det].

[44] E. Richter-Was, D. Froidevaux, and L. Poggioli, *ATLFAST 2.0 a fast simulation package for ATLAS*, ATL-PHYS-98-131, 1998.

[45] ATLAS Collaboration, M. Beckingham, M. Duehrssen, E. Schmidt, M. Shapiro, et al., *The simulation principle and performance of the ATLAS fast calorimeter simulation FastCaloSim*, ATL-PHYS-PUB-2010-013, 2010.

[46] T. Sjostrand, S. Mrenna, and P. Skands, *PYTHIA 6.4 physics and manual*, JHEP **0605** (2006) 026, `arXiv:hep-ph/0603175`.

[47] S. Frixione and B. R. Webber, *Matching NLO QCD computations and parton shower simulations*, JHEP **0206** (2002) 029.

[48] S. Frixione, P. Nason, and B. R. Webber, *Matching NLO QCD and parton showers in heavy flavour production*, JHEP **0308** (2003) 007.

[49] S. Frixione, E. Laenen, P. Motylinski, and B. R. Webber, *Single-top production in MC@NLO*, JHEP **0603** (2006) 092.

[50] S. Frixione, P. Nason, and C. Oleari, *Matching NLO QCD computations with Parton Shower similations: the POWHEG method*, JHEP **0711** (2007) 070.

[51] M. L. Mangano, M. Moretti, F. Piccinini, R. Pittau, and A. D. Polosa, *ALPGEN, a generator for hard multiparton processes in hadronic collisions*, JHEP **0307** (2003) 001, `arXiv:hep-ph/0206293`.

[52] G. Corcella et al., *HERWIG 6: An event generator for hadron emission reactions with interfering gluons (including supersymmetric processes)*, JHEP **0101** (2001) 010, `arXiv:hep-ph/0011363`.

[53] M. Aliev et al., *HATHOR: HAdronic Top and Heavy quarks crOss section calculatoR*, Comput. Phys. Commun. **182** (2011) 1034–1046, `arXiv:1007.1327 [hep-ph]`.

[54] B. P. Kersevan and E. Richter-Was, *The Monte Carlo event generator AcerMC version 2.0 with interfaces to PYTHIA 6.2 and HERWIG 6.5*, `arXiv:hep-ph/0405247`.

[55] T. Gleisberg et al., *Event generation with SHERPA 1.1*, JHEP **0902** (2009) 007.

[56] S. Catani, L. Cieri, G. Ferrera, D. de Florian, and M. Grazzini, *Vector boson production at hadron colliders: A Fully exclusive QCD calculation at NNLO*, Phys. Rev. Lett. **103** (2009) 082001, `arXiv:0903.2120 [hep-ph]`.

[57] T. Binoth, M. Ciccolini, N. Kauer, and M. Kramer, *Gluon-induced W-boson pair production at the LHC*, JHEP **0612** (2006) 046, `arXiv:hep-ph/0611170`.

[58] T. Binoth, N. Kauer, and P. Mertsch, *Gluon-induced QCD corrections to $pp \to ZZ \to \ell\bar{\ell}\ell'\bar{\ell}'$*, `arXiv:0807.0024 [hep-ph]`.

[59] J. M. Campbell and R. K. Ellis, *An Update on vector boson pair production at hadron colliders*, Phys. Rev. **D60** (1999) 113006, `arXiv:hep-ph/9905386`.

[60] J. M. Campbell, R. K. Ellis, and C. Williams, *Vector boson pair production at the LHC*, JHEP **1107** (2011) 018, `arXiv:1105.0020 [hep-ph]`.

[61] J. Alwall, M. Herquet, F. Maltoni, O. Mattelaer, and T. Stelzer, *MadGraph 5 : Going Beyond*, JHEP **1106** (2011) 128, `arXiv:1106.0522 [hep-ph]`.

[62] A. Lazopoulos, T. McElmurry, K. Melnikov, and F. Petriello, *Next-to-leading order QCD corrections to $t\bar{t}Z$ production at the LHC*, Phys. Lett. **B666** (2008) 62–65, `arXiv:0804.2220 [hep-ph]`.

[63] J. M. Campbell and R. K. Ellis, *$t\bar{t}W^{\pm}$ production and decay at NLO*, JHEP **1207** (2012) 052, `arXiv:1204.5678 [hep-ph]`.

[64] M. Garzelli, A. Kardos, C. Papadopoulos, and Z. Trocsanyi, *$t\bar{t} W^{\pm}$ and $t\bar{t} Z$ hadroproduction at NLO accuracy in QCD with parton shower and hadronization effects*, JHEP **1211** (2012) 056, `arXiv:1208.2665 [hep-ph]`.

[65] J. Butterworth, J. Forshaw, and M. Seymour, *Multiparton interactions in photoproduction at HERA*, Z. Phys. **C72** (1996) 637–646, `hep-ph/9601371`.

[66] H.-L. Lai, M. Guzzi, J. Huston, Z. Li, P. M. Nadolsky, et al., *New parton distributions for collider physics*, Phys. Rev. **D82** (2010) 074024, `arXiv:1007.2241 [hep-ph]`.

[67] J. Pumplin, D. Stump, J. Huston, H. Lai, P. M. Nadolsky, et al., *New generation of parton distributions with uncertainties from global QCD analysis*, JHEP **0207** (2002) 012, arXiv:hep-ph/0201195 [hep-ph].

[68] M. Bahr et al., *Herwig++ Physics and Manual*, Eur. Phys. J. **C58** (2008) 639–707, arXiv:0803.0883 [hep-ph].

[69] W. Beenakker, R. Hopker, M. Spira, and P. M. Zerwas, *Squark and gluino production at hadron colliders*, Nucl. Phys. **B492** (1997) 51–103, arXiv:hep-ph/9610490.

[70] S. AbdusSalam et al., *Benchmark Models, Planes, Lines and Points for Future SUSY Searches at the LHC*, arXiv:1109.3859 [hep-ph].

[71] ATLAS Collaboration, *Electron performance measurements with the ATLAS detector using the 2010 LHC proton-proton collision data*, Eur. Phys. J. **C72** (2012) 1909, arXiv:1110.3174 [hep-ex].

[72] M. Cacciari, G. P. Salam, and G. Soyez, *The anti-k_T jet clustering algorithm*, JHEP **0804** (2008) 063, arXiv:0802.1189 [hep-ph].

[73] M. Cacciari and G. P. Salam, *Dispelling the N^3 myth for the k_t jet-finder*, Phys. Lett. **B641** (2006) 57–61, arXiv:hep-ph/0512210 [hep-ph].

[74] ATLAS Collaboration, G. Aad et al., *Jet energy measurement with the ATLAS detector in proton-proton collisions at $\sqrt{s}$ = 7 TeV*, Eur. Phys. J. **C73** (2013) 2304, arXiv:1112.6426 [hep-ex].

[75] ATLAS Collaboration, *Commissioning of the ATLAS high-performance b-tagging algorithms in the 7 TeV collision data*, ATLAS-CONF-2011-102, http://cdsweb.cern.ch/record/1369219.

[76] ATLAS Collaboration, *Measurement of the WW cross section in $\sqrt{s}$ = 7 TeV pp collisions with ATLAS*, Phys. Rev. Lett. **107** (2011) 041802, arXiv:1104.5225 [hep-ex].

[77] C. G. Lester and D. J. Summers, *Measuring masses of semiinvisibly decaying particles pair produced at hadron colliders*, Phys. Lett. **B463** (1999) 99–103, arXiv:hep-ph/9906349.

[78] A. Barr, C. Lester, and P. Stephens, *m_{T2} : The Truth behind the glamour*, J. Phys. **G29** (2003) 2343–2363, arXiv:hep-ph/0304226.

[79] ATLAS Collaboration, *Measurements of the properties of the Higgs-like boson in the $WW^{(*)} \rightarrow l\nu l\nu$ decay channel with the ATLAS detector using 25 fb^{-1} of proton-proton collision data*, ATLAS-CONF-2013-030, http://cds.cern.ch/record/1527126.

[80] ATLAS Collaboration, *Measurement of the top quark-pair production cross section with ATLAS in pp collisions at $\sqrt{s}$ = 7 TeV*, Eur. Phys. J. **C71** (2011) 1577, arXiv:1012.1792 [hep-ex].

[81] G. Cowan, K. Cranmer, E. Gross, and O. Vitells, *Asymptotic formulae for likelihood-based tests of new physics*, Eur. Phys. J. **C71** (2011) 1554, arXiv:1007.1727 [physics.data-an].

[82] ATLAS Collaboration, *Jet energy measurement with the ATLAS detector in proton-proton collisions at $\sqrt{s}$ = 7 TeV*, Eur. Phys. J. **C73** (2013) 2304, arXiv:1112.6426 [hep-ex].

[83] ATLAS Collaboration, *Jet energy scale and its systematic uncertainty in proton-proton collisions at $\sqrt{s}$ = 7 TeV with ATLAS 2011 data*, ATLAS-CONF-2013-004, http://cds.cern.ch/record/1509552.

[84] ATLAS Collaboration, *In situ jet pseudorapidity intercalibration of the ATLAS detector using dijet events in $\sqrt{s}$ = 7 TeV proton-proton 2011 data*, ATLAS-CONF-2012-124, http://cds.cern.ch/record/1474490.

[85] ATLAS Collaboration, *Pile-up corrections for jets from proton-proton collisions at $\sqrt{s}$ = 7 TeV in ATLAS in 2011*, ATLAS-CONF-2012-064, http://cds.cern.ch/record/1459529.

[86] ATLAS Collaboration, *Probing the measurement of jet energies with the ATLAS detector using photon+jet events in proton-proton collisions at $\sqrt{s}$ = 7 TeV*, ATLAS-CONF-2012-063, http://cds.cern.ch/record/1459528.

[87] ATLAS Collaboration, *Probing the measurement of jet energies with the ATLAS detector using Z+jet events from proton-proton collisions at $\sqrt{s}$ = 7 TeV*, ATLAS-CONF-2012-053, http://cds.cern.ch/record/1452641.

[88] ATLAS Collaboration, *Jet energy resolution in proton-proton collisions at $\sqrt{s}$ = 7 TeV recorded in 2010 with the ATLAS detector*, Eur. Phys. J. **C73** (2013) 2306, arXiv:1210.6210 [hep-ex].

[89] ATLAS Collaboration, *Muon reconstruction efficiency in reprocessed 2010 LHC p-p collision data recorded with the ATLAS detector*, ATLAS-CONF-2011-063, http://cds.cern.ch/record/1345743.

[90] ATLAS Collaboration, *A measurement of the muon reconstruction efficiency in 2010 ATLAS data using j/psi decays*, ATLAS-CONF-2012-125, https://cds.cern.ch/record/1474642.

[91] ATLAS Collaboration, *ATLAS Muon Momentum Resolution in the First Pass Reconstruction of the 2010 p-p Collision Data at $\sqrt{s}$ = 7 TeV*, ATLAS-CONF-2011-046, http://cds.cern.ch/record/1338575.

[92] ATLAS Collaboration, *Measuring the b-tag efficiency in a ttbar sample with 4.7 fb^{-1} of data from the ATLAS detector*, ATLAS-CONF-2012-097, http://cds.cern.ch/record/1460443.

[93] ATLAS Collaboration, *Improved luminosity determination in pp collisions at $\sqrt{s}$ = 7 TeV using the ATLAS detector at the LHC*, arXiv:1302.4393 [hep-ex].

[94] M. Kramer et al., *Supersymmetry production cross sections in pp collisions at $\sqrt{s}$ = 7 TeV*, arXiv:1206.2892 [hep-ph].

[95] A. L. Read, *Presentation of search results: The CL_s technique*, J. Phys. **G28** (2002) 2693–2704.
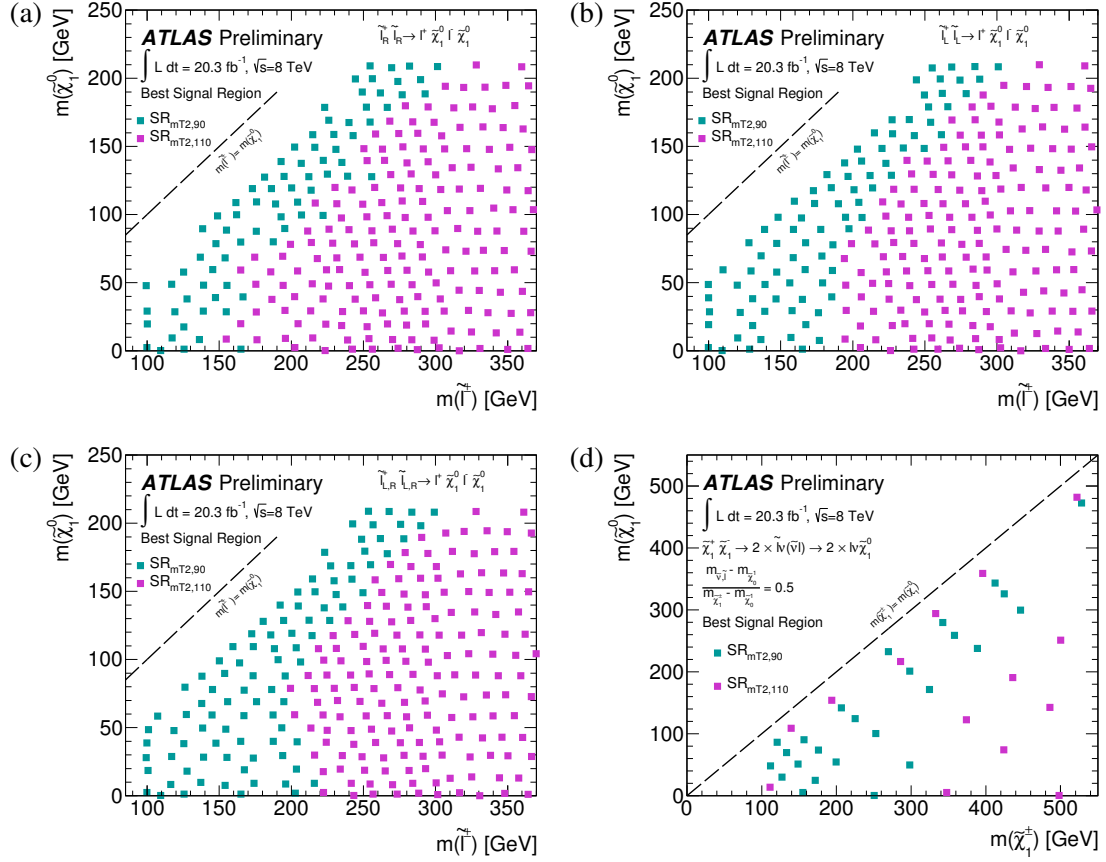
Additional Material

Figure 10: Signal regions contributing to the exclusion limit in the plane of (a) slepton mass and the lightest neutralino mass for combined right-handed selectrons and smuons, (b) slepton mass and the lightest neutralino mass for combined left-handed selectrons and smuons, (c) slepton mass and the lightest neutralino mass for combined left-handed and right-handed selectrons and smuons, and (d) chargino mass and the lightest neutralino mass. The different colors show which signal region, SR-$m_{\text{T2},90}$ or SR-$m_{\text{T2},110}$, has the highest expected sensitivity at a given mass point.
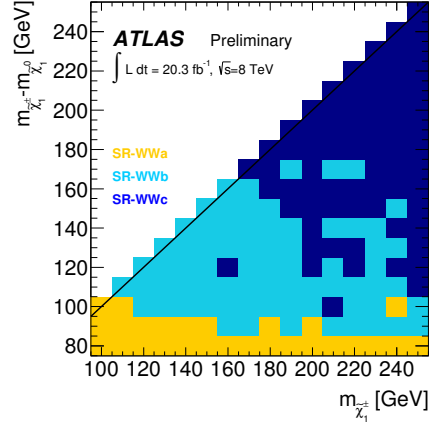
Figure 11: Signal regions contributing to the exclusion limit in the $m_{\tilde{\chi}_1^0}$–$m_{\tilde{\chi}_1^\pm}$ plane. The different colors show which signal region, SR-WWa, SR-WWb or SR-WWc, has the highest expected sensitivity at a given mass point.
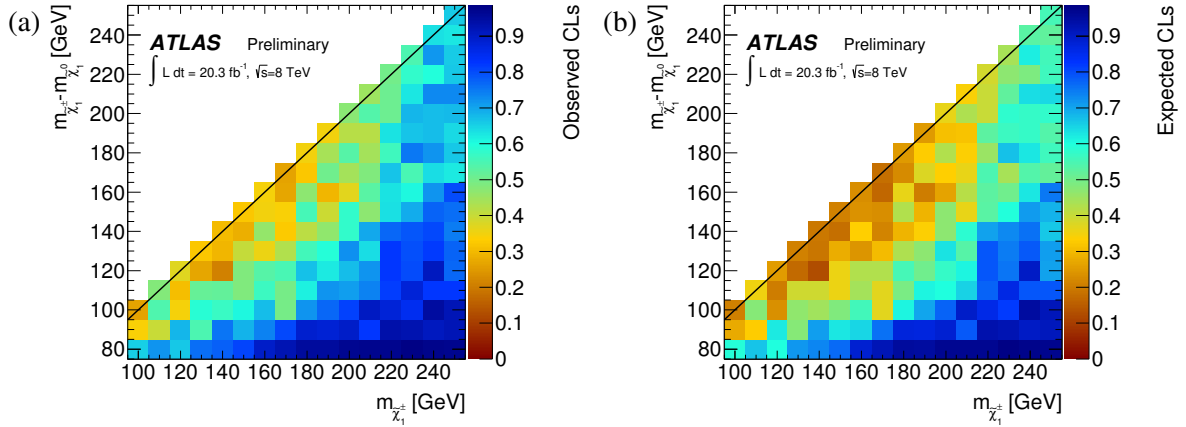

Figure 12: Observed (a) and expected (b) CL$_s$ values from SR-WWa–c for simplified models with bino-like $\tilde{\chi}_1^0$ and wino-like $\tilde{\chi}_1^\pm$ in the $m_{\tilde{\chi}_1^0}$–$m_{\tilde{\chi}_1^\pm}$ plane.

$(m_{\tilde{\ell}}, m_{\tilde{\chi}_1^0})$	(191, 90) GeV		(250, 10) GeV	
Lepton flavour	e^+e^-	$\mu^+\mu^-$	e^+e^-	$\mu^+\mu^-$
Trigger	150	159	55	50
Z veto	139	148	54	49
Jet veto	58	62	20	20
$E_T^{miss,rel}$	45	50	17	17
SR-$m_{T2,90}$	21.6	21.6	12.2	12.5
SR-$m_{T2,110}$	12.3	12.0	10.5	11.2

Table 6: Expected numbers of signal events after each step of the event selection for slepton-pair production benchmark model points, $(m_{\tilde{\ell}}, m_{\tilde{\chi}_1^0}) = (191, 90)$ GeV and $(250, 10)$ GeV, with common left- and right-handed slepton masses. A total of 5000 events are generated in each sample. The numbers are scaled to correspond to an integrated luminosity of 20.3 fb^{-1}.
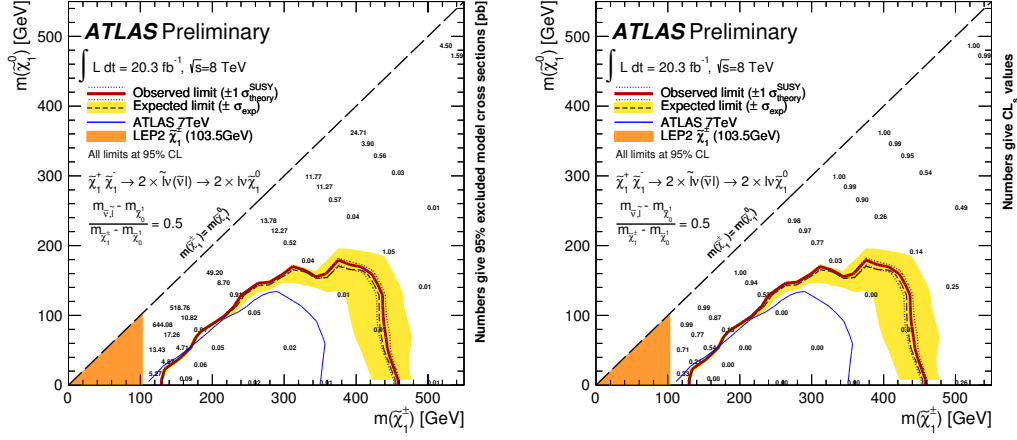
Figure 13: 95% exclusion limit for the mode with intermediary sleptons in the plane with the chargino mass and the lightest neutralino mass. (Left) The numbers in the plot quote the 95% CL excluded limits on the model cross section in pb. (Right) The number in the plot quote the CL_s value at a given mass point.
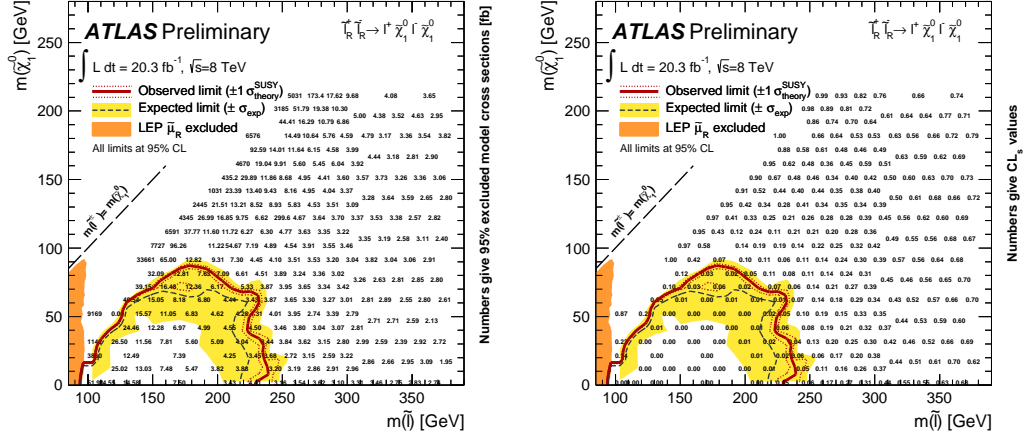

Figure 14: 95% exclusion limit for combined right-handed selectrons and smuons. (Left) The numbers in the plot quote the 95% CL excluded limits on the model cross section in fb. (Right) The number in the plot quote the CL_s value at a given mass point.
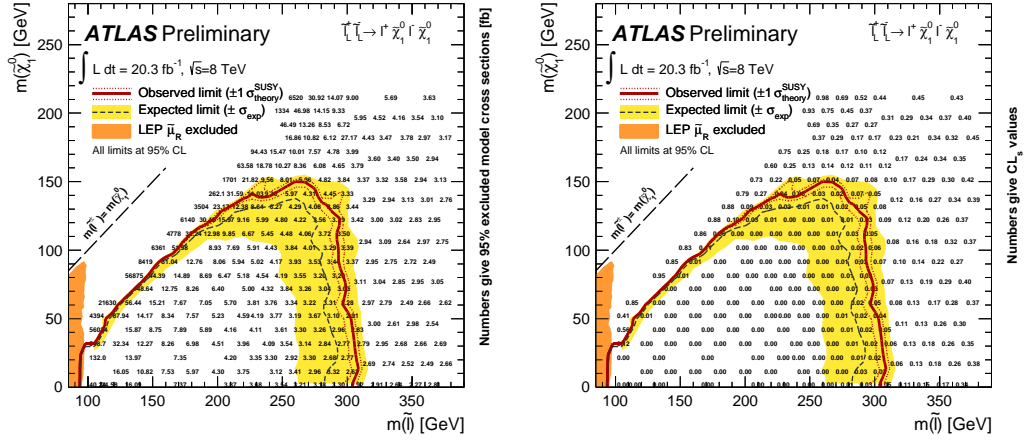
Figure 15: 95% exclusion limit for combined left-handed selectrons and smuons. (Left) The numbers in the plot quote the 95% CL excluded limits on the model cross section in fb. (Right) The number in the plot quote the CL_s value at a given mass point.
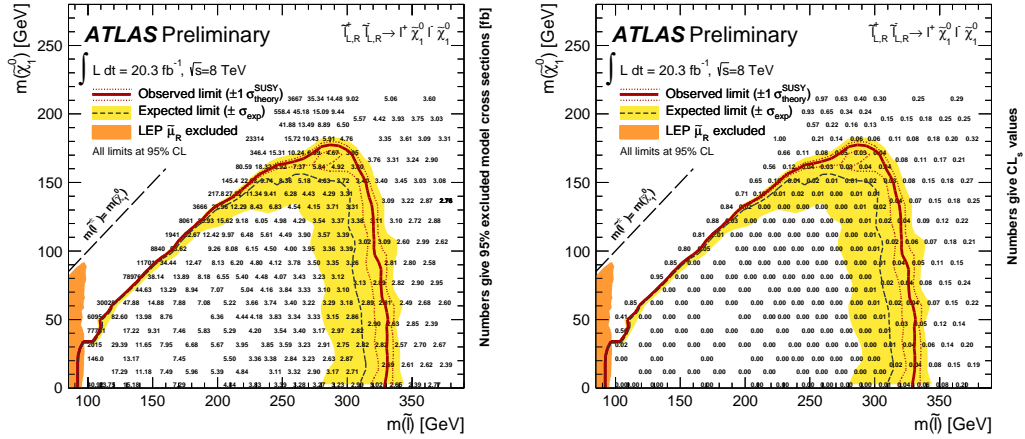

Figure 16: 95% exclusion limit for combined right-handed and left-handed selectrons and smuons. (Left) The numbers in the plot quote the 95% CL excluded limits on the model cross section in fb. (Right) The number in the plot quote the CL_s value at a given mass point.

$(m_{\tilde{\chi}_1^\pm}, m_{\tilde{\chi}_1^0})$	(350, 0) GeV			(425, 75) GeV		
Lepton flavour	e^+e^-	$\mu^+\mu^-$	$e^\pm\mu^\mp$	e^+e^-	$\mu^+\mu^-$	$e^\pm\mu^\mp$
Trigger	52	48	79	20	20	31
Z veto	48	45	74	19	19	29
Jet veto	20	19	30	7	7	11
$E_{\mathrm{T}}^{\mathrm{miss,rel}}$	17	17	25	6	6	9
SR-$m_{\mathrm{T2,90}}$	11.7	10.5	16.6	4.3	4.4	6.7
SR-$m_{\mathrm{T2,110}}$	9.5	8.7	14.0	3.7	3.8	5.7

Table 7: Expected numbers of signal events after each step of the event selection for chargino-pair production with intermediary slepton benchmark model points, $(m_{\tilde{\chi}_1^\pm}, m_{\tilde{\chi}_1^0})$ = (350, 0) GeV and (425, 75) GeV. A total of 40000 events are generated in each sample. The numbers are scaled to correspond to an integrated luminosity of 20.3 fb^{-1}.

Signal model	S1	S2	S3	GMSB
No Cuts	11003	3393	749	10239
All cleaning	10691	3299	732	10066
Two signal leptons	3178	1060	261	3960
Trigger	2559	872	214	3097
$e^\pm\mu^\mp$	861	296	71	661
Jet veto	443	139	31	241
$(p_{\mathrm{T}}^{\ell1}, p_{\mathrm{T}}^{\ell2} > (35, 20)$ GeV	310	103	25	167
SR-WWa	31.5			18.2
SR-WWb		8.2		4.3
SR-WWc			3.3	

Table 8: Expected numbers of signal events after each step of the event selection for benchmark model points in the SR-WW. The numbers are scaled to correspond to an integrated luminosity of 20.3 fb^{-1}. The signal models S1, S2 and S3 are chargino-pair production with wino-like $\tilde{\chi}_1^\pm$ and bino-like $\tilde{\chi}_1^0$ with $(m_{\tilde{\chi}_1^\pm}, m_{\tilde{\chi}_1^0})$ = (100, 0) GeV, (140, 20) GeV and (200, 0) GeV, respectively. The GMSB model has $m_{\tilde{\chi}_1^\pm}$ = 110 GeV, $m_{\tilde{\chi}_1^0}$ = 113 GeV, and the LSP is a massless gravitino.